

## Re-examination of the SiGe Raman spectra: Percolation/one-dimensional-cluster scheme and *ab initio* calculations

O. Pagès,<sup>1,\*</sup> J. Souhabi,<sup>1</sup> V. J. B. Torres,<sup>2</sup> A. V. Postnikov,<sup>1</sup> and K. C. Rustagi<sup>3</sup><sup>1</sup>*Laboratoire de Chimie et Physique—Approche Multi-Echelle des Milieux Complexes, Institut Jean Barriol, Université de Lorraine, 57078 Metz, France*<sup>2</sup>*Departamento de Física and I3N, Universidade de Aveiro, Campus Santiago, 3810-193, Aveiro, Portugal*<sup>3</sup>*Indian Institute of Technology, Powai, Mumbai, 400076, India*

(Received 5 April 2011; revised manuscript received 16 May 2012; published 5 July 2012)

We report on the detailed assignment of various features observed in the Raman spectra of SiGe alloys along the linear chain approximation (LCA), as achieved based on remarkable intensity interplays with composition between such neighboring features known from the literature but which so far have not been fully exploited. Such an assignment is independently supported by *ab initio* calculation of the frequencies of bond-stretching modes taking place in different local environments, which we define at one dimension (1D) for consistency with the LCA. Fair contour modeling of the SiGe Raman spectra is eventually obtained via a so-called 1D-cluster version of the phenomenological (LCA-based) percolation scheme, as originally developed for zincblende alloys, after *ab initio* calibration of the intrinsic Si-Si, Si-Ge, and Ge-Ge Raman efficiencies. The 1D-cluster scheme introduces a seven-oscillator [ $1 \times (\text{Ge-Ge})$ ,  $4 \times (\text{Si-Ge})$ ,  $2 \times (\text{Si-Si})$ ] Raman behavior for SiGe, which considerably deviates from the currently accepted six-oscillator [ $1 \times (\text{Ge-Ge})$ ,  $1 \times (\text{Si-Ge})$ ,  $4 \times (\text{Si-Si})$ ] behavior. Different numbers of Raman modes per bond are interpreted as different sensitivities to the local environment of Ge-Ge (insensitive), Si-Si (sensitive to first neighbors), and Si-Ge (sensitive to second neighbors) bond stretching. The as-obtained SiGe 1D-cluster/percolation scheme is also compared with the current version for zincblende alloys, using GaAsP as a natural reference. A marked deviation is concerned with an inversion of the like phonon branches in each multiplet. This is attributed either to the considerable Si and Ge phonon dispersions (Si-Si doublet) or to a basic difference in the lattice relaxations of diamond and zincblende alloys (Si-Ge multiplet). The SiGe vs GaAsP comparison is supported by *ab initio* calculation of the local lattice relaxation/dynamics related to prototype impurity motifs that are directly transposable to the two crystal structures.

DOI: [10.1103/PhysRevB.86.045201](https://doi.org/10.1103/PhysRevB.86.045201)

PACS number(s): 63.50.Gh, 63.10.+a, 63.20.Pw

### I. INTRODUCTION

Since the emergence of semiconductor alloys some six decades ago, the physical properties of  $\text{Si}_{1-x}\text{Ge}_x$ , the leading group IV alloy with a diamond structure, have by far attracted the most attention, both experimentally and theoretically.<sup>1</sup> The current semiconductor technology is essentially based on Si; therefore, any possible way to play with the intrinsic physical properties of Si (i.e., by alloying, in the present case) is potentially interesting and as such is methodically scrutinized. Moreover, among all possible Si-related group IV (C, Si, Ge, and Sn) binary alloys,  $\text{Si}_{1-x}\text{Ge}_x$  seems to be the only exception of a random alloy that retains the diamond structure of the parents throughout the composition domain. This is because the contrast in the bond lengths ( $l$ ) and in the bond-stretching ( $\alpha$ ) and bond-bending ( $\beta$ ) force constants of the constituent species remains rather moderate in SiGe ( $\Delta l \approx 4\%$ ,  $\Delta\alpha \approx 15\%$ , and  $\Delta\beta \approx 12\%$ ), whereas it becomes prohibitive for the next SiC candidate ( $\sim 34\%$ ,  $\sim 58\%$ , and  $\sim 83\%$ , respectively) and SiSn candidate ( $\sim 17\%$ ,  $\sim 41\%$ , and  $\sim 53\%$ , respectively).<sup>2,3</sup> On the technical side, a current application of major importance is that relaxed epilayers of SiGe can serve as a substrate for strained epilayers of Si,<sup>4,5</sup> which are then used for high-mobility devices (Refs. 6 and 7).

In this work, we are interested in the SiGe vibrational properties, as detected by Raman scattering. While this technique operates at the Brillouin zone center (BZC), and as such restricts the analysis to long-wavelength optical phonons ( $q \approx 0$ ), these are detected with a very high resolution,

sometimes better than  $\sim 1 \text{ cm}^{-1}$ . This is less, by at least a factor of 2, than the typical width at half maximum of the Raman line of a pure Si crystal.<sup>8</sup> As such, Raman scattering is the best technique when searching to access the detail of the phonon mode behavior of a complex system such as an alloy.

For direct insight into the  $\text{Si}_{1-x}\text{Ge}_x$  Raman spectra, we reproduce in the main panel of Fig. 1 a representative set taken by Alonso and Winer with epitaxial layers covering well-spanned alloy compositions ( $x \approx 0.25, 0.50$ , and  $0.75$ , taken from Fig. 2 of Ref. 9). Three main Ge-Ge, Si-Ge, and Si-Si Raman features, underscored in the main panel of Fig. 1, emerge at intermediate composition ( $x \approx 0.55$ ). When the alloy composition varies, the low-frequency ( $\sim 300 \text{ cm}^{-1}$ ) and high-frequency ( $\sim 500 \text{ cm}^{-1}$ ) features connect to the modes of the pure Si and Ge crystals, respectively. Their assignment in terms of the main Ge-Ge and Si-Si modes is thus straightforward. The intermediate mode is intimately related to a mode observed in Si/Ge superlattices and in multiple quantum well structures when the Si/Ge interface is rough.<sup>10,11</sup> This naturally leads to an assignment in terms of the main Si-Ge mode.

The main Ge-Ge and Si-Si modes exhibit opposite shifts when the Ge content increases, i.e., upward and downward, respectively, while the intermediate Si-Ge mode remains more or less stationary. Detailed modeling of the composition dependence of the frequencies of the main Ge-Ge, Si-Ge and Si-Si Raman features was performed by Sui *et al.* using a modified cellular isodisplacement model.<sup>12</sup> The opposite Ge-Ge and Si-Si shifts were investigated by Rucker and

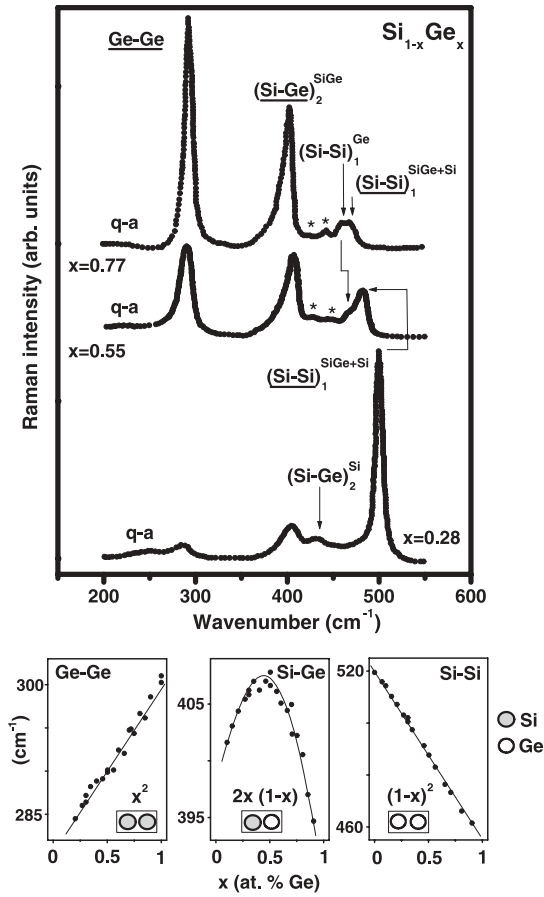


FIG. 1. Main SiGe Raman features. Representative  $\text{Si}_{1-x}\text{Ge}_x$  Raman spectra taken by Alonso and Winer (plain symbols, digitalized from Fig. 2 of Ref. 9) are shown in the main panel. In the minor panels are summarized the  $x$  dependencies proposed by Pezzoli *et al.* for the frequency (plain symbols, digitalized from Fig. 2 of Ref. 13, visual guides added) and intensity (in reference to the indicated fractions of related oscillators) of the main Ge-Ge, Si-Ge, and Si-Si Raman features (underscored in the main panel). Each of these is assigned a specific bond-stretching oscillator (refer to the symbolic notation with two atoms in a box in each minor panel). We introduce more general labeling of the Raman features, according to the symbolic notation  $(X)_Y^Z$ , covering both the main (underscored in the main panel) and the minor (not underscored) Raman features and corresponding to a given bond stretching ( $X$ ) in a given 1D environment as characterized by its microstructure (superscript  $Y$ : in reference to Ge-, SiGe-, or Si-like environments) and length scale (subscript  $Z$ : standing for 1 or 2 in reference to first and second neighbors, respectively). The corresponding oscillators are represented in the body of Fig. 4 (refer to letters a – f in the figure image), using the same symbolic notation as in the present figure, for a direct comparison. The minor  $(\text{Si-Ge})_2^{\text{Si-Ge}}$  feature (bottom spectrum in the main panel) decomposes into a pseudodoublet away from the Ge-dilute/moderate limit, corresponding to the features highlighted by asterisks in the upper two spectra. The q-a notation refers to a parasitical quasiamorphous feature.

Methfessel (Ref. 3) by using a supercell approach and an anharmonic version of the Keating model, in which changes in the bond-stretching and bond-bending force constants depending on the local bond distortion were taken into account. The confinement and microscopic strain effects were

found to add for the main Si-Si mode, corresponding to drastic phonon softening (red-shift) when the Ge content increases. In contrast, the two effects oppose for the main Ge-Ge mode, to the advantage of the confinement effect, leading to slight phonon hardening (blue-shift) with increasing Ge content. Such competition between the confinement and the microscopic strain effects is discussed later. As for the intensities of the main Ge-Ge, Si-Ge, and Si-Si Raman lines, Pezzoli *et al.*<sup>13</sup> proposed empirical laws indicating a basic scaling with the bond fractions when assuming a random  $\text{Si} \leftrightarrow \text{Ge}$  substitution, i.e., according to  $(1-x)^2$ ,  $2x \cdot (1-x)$ , and  $x^2$ , respectively. Such scaling implies that at a given alloy composition, the bonds of a given species vibrate at the same frequency whatever their local environment, being thus all equivalent. The individual bond-stretching oscillators behind such main Ge-Ge, Si-Ge, and Si-Si modes are merely defined at the bond scale, with no information on the local environment. A schematic representation is given in specific panels at the bottom of Fig. 1, in which the frequency (plain circles, taken from Fig. 2 of Ref. 13) and intensity (see text and Fig. 3 of Ref. 13) aspects are summarized per mode.

Careful examination of the SiGe Raman spectra in Fig. 1 reveals two minor features (not underscored) besides the main Ge-Ge, Si-Ge, and Si-Si ones (underscored). An additional minor feature is discussed later. The assignment of the minor features has attracted considerable attention over the last four decades, both experimentally<sup>9,14–17</sup> and theoretically.<sup>9,17–23</sup> Some representative data are regrouped into a composite frequency map in Fig. 2(a), with their assignments recapitulated in Fig. 2(b). Such assignments were achieved based on sophisticated phonon calculations as performed in the real three-dimensional (3D) crystal, searching for frequency matching between a given Raman line and the vibration of a given atom (Si or Ge) taken in some likely 3D environment at the considered alloy composition. In retrospect, it seems that it was tacitly admitted that any 3D environment should be limited to first neighbors only. Accordingly, we adopt a uniform  $A_n$  notation for all 3D assignments in Fig. 2(b), corresponding to an atom  $A$  (Si or Ge, respectively) vibrating in presence of  $n$  ( $n = 0–4$ ) first neighbors of the like species (Si or Ge, respectively). The additional information about the intensities of the main Ge-Ge, Si-Ge, and Si-Si Raman lines, as empirically derived by Pezzoli *et al.* (explained earlier),<sup>13</sup> is included for completeness in Fig. 2(b) via appropriate thickening of the relevant phonon branches. As such, we can say that Fig. 2(b) summarizes the current understanding of the SiGe Raman spectra.

The pioneering  $\text{Si}_{1-x}\text{Ge}_x$  Raman spectra were obtained with polycrystals by Feldman *et al.*<sup>14</sup> at moderate Si content ( $0.75 \leq x \leq 1$ ) and by Renucci *et al.*<sup>24</sup> and Brya<sup>15</sup> throughout the composition domain. Several interesting Raman features were identified. Preliminary indication regarding the origin of the emerging features at the Si- and Ge-dilute limits was given by Dawber and Elliott (Ref. 18), Montroll and Potts (Ref. 23), and Maradudin<sup>19</sup> using theories applicable to isolated impurities only. In particular, a long-standing enigma, originally raised by Brya<sup>15</sup> and taken up again by Taylor<sup>25</sup> in his review on the Raman spectra of alloys, is that the main Si-Ge line does not connect with any predicted modes for an isolated Ge atom, in reference to the two potential

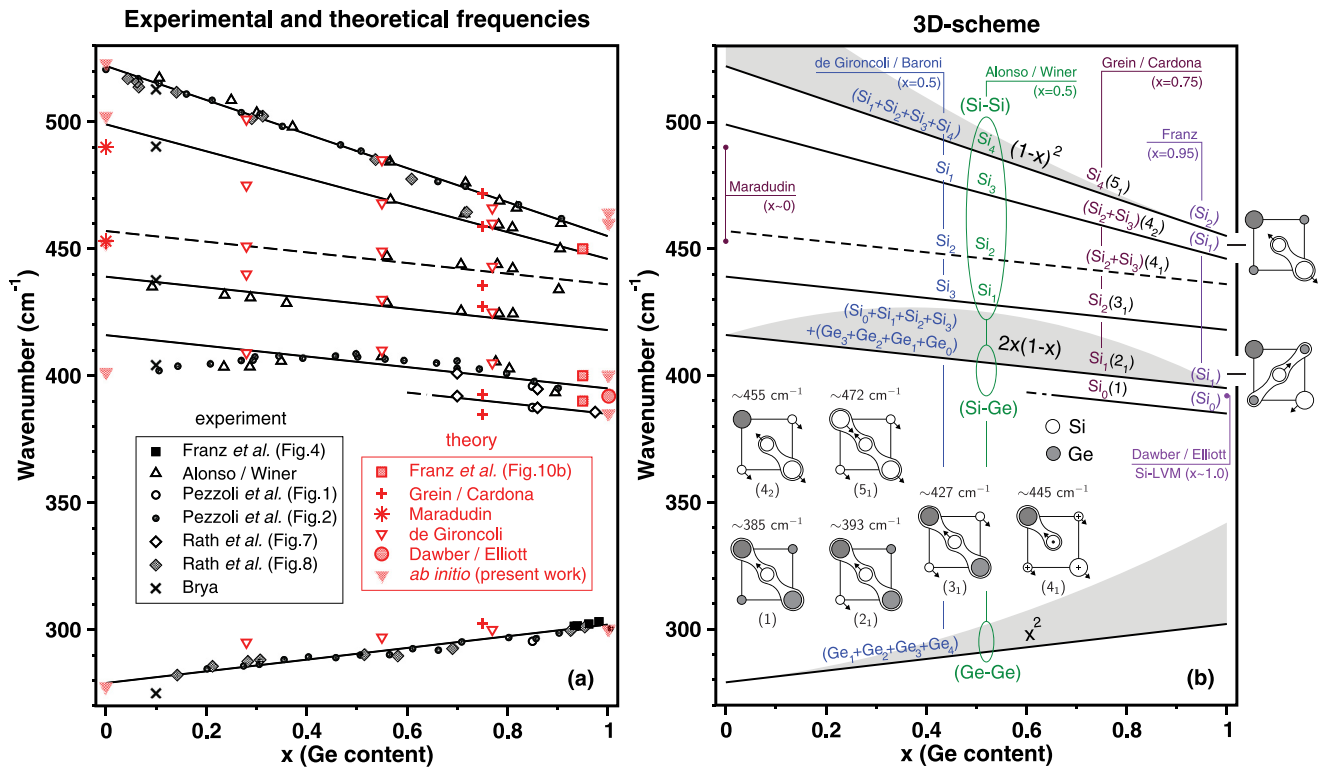


FIG. 2. (Color online) SiGe Raman spectra. Si<sub>1-x</sub>Ge<sub>x</sub> Raman frequency map, including (a) raw experimental data (black symbols; cited data are from Refs. 9, 13, and 15–17) and theoretical data (gray (red online) symbols; cited data are from Refs. 17–21) from the literature (straight lines are visual guides), and (b) corresponding assignment of the Raman modes within the current six-oscillator [1 × (Ge-Ge), 1 × (Si-Ge), 4 × (Si-Si)] 3D scheme. The like phonon branches, referring to the same bond stretching, are regrouped by ovals. The individual assignments are recapitulated by adopting a uniform A<sub>n</sub> notation. This refers to an atom A (Si or Ge) vibrating in presence of n A-like atoms (n = 0–4) in its nearest-neighbor shell. The corresponding vibration patterns, as identified by Grein and Cardona within their mass-defect Green’s function approach (Ref. 20), are schematically reproduced in panel (b), emphasizing bond stretching. A standard notation is used for backward (⊕) and upward (⊙) atomic motions. The N<sub>M</sub> labeling of these authors, referring to the Mth vibration mode in the sense of increasing frequency of a cluster of N Si atoms, is preserved for direct correspondence with the original patterns (given in Fig. 4 of Ref. 20). The individual bond fractions, which monitor the intensities of the main Raman lines (see text) following Pezzoli *et al.* (Ref. 13), are added for completeness. They are specified on top of each relevant branch and visualized via appropriate thickening of such branches (gray areas in panel (b)).

candidates predicted by Maradudin<sup>19</sup> (Fig. 2) for the local vibration modes (LVMs) of Ge in Si (Ge-LVM, Ge<sub>0</sub>). At intermediate composition, where the existing theories could not apply, three distinct minor features were identified between the main Si-Ge and the main Si-Si Raman features. They were tentatively assigned by Brya<sup>15</sup> as reminiscent of modes already detected in the Si-dilute (~448 cm<sup>-1</sup>) and Ge-dilute (~437 and ~487 cm<sup>-1</sup>) limits, which show little change in frequency or intensity when the composition changes.

The next generation of data or assignments brings together the considerable experimental<sup>9</sup> and theoretical<sup>9,20–22</sup> efforts conducted before the mid-1990s to understand the puzzling multimode Raman pattern at intermediate composition.<sup>15</sup> Such studies benefited both from the arrival of a novel generation of samples, grown as single crystals, and from the emergence of novel theoretical methods that could treat all the statistics of the atom substitution behind the alloy disorder realistically. Details follow.

Alonso and Winer (Ref. 9) reported the first detailed Raman study of intermediate alloy compositions. The interpretation of their data was supported by a Keating model supercell (216-atom) calculation assuming stable force constants in a

first approximation. These were estimated from the elastic constants of the pure Si and Ge crystals,<sup>2</sup> taking geometrical means for the Si-Ge mixed bond. Reference calculations were performed with an ordered Si<sub>0.5</sub>Ge<sub>0.5</sub> crystal corresponding to alternate pairs of Si and Ge (111) planes. The crucial result is that only the disordered supercells generated the experimentally observed minor features between the main Si-Ge and the main Si-Si features. The trend was confirmed by an experimental observation that the minor features show up with bulk polycrystals,<sup>9,14,15</sup> as well as with relaxed epitaxial layers,<sup>9,13,16,17</sup> i.e., independently of the growth process. The origin of the minor features was further discussed on the microscopic scale by focusing on the central minor peak at intermediate composition (x = 0.55). This was attributed to Si-Si bond stretching in a Si-centered tetrahedron unit with equal numbers (2) of Si and Ge atoms at the vertices (Si<sub>2</sub>, ~450 cm<sup>-1</sup>). The softening with respect to Si-Si stretching in the pure Si crystal (Si<sub>4</sub>, ~520 cm<sup>-1</sup>), corresponding to the main Si-Si Raman feature in the alloy (Si<sub>4</sub>, ~480 cm<sup>-1</sup>), was attributed to a confinement effect due to the quasi-inert Ge atoms with a large mass. By extension, the three remaining minor peaks were assigned, in the sense of decreasing

frequency, to increasingly confined Si-Si bond stretching in Si-centered tetrahedron units with increasing numbers of Ge atoms at the vertices, i.e., from one ( $\text{Si}_3$ ,  $\sim 470 \text{ cm}^{-1}$ ) to three ( $\text{Si}_1$ ,  $\sim 430 \text{ cm}^{-1}$ ). *Altogether, this yields the standard description of the SiGe Raman pattern with six bond-stretching oscillators [ $1 \times (\text{Ge-Ge})$ ,  $1 \times (\text{Si-Ge})$ ,  $4 \times (\text{Si-Si})$ ], except that the order of the Si-Si modes may vary, as described later. The oscillators of like nature, i.e., referring to the same ultimate bond stretching, are regrouped using ovals in Fig. 2(b) for a better insight.*

Grein and Cardona (Ref. 20) used a mass-defect Green's function approach to calculate the SiGe Raman spectra at moderate Si content (25 at.%), where the minor Raman features show up clearly. The alloy was ideally described in terms of a collection of Si- and Ge-centered tetrahedron units embedded in a uniform continuum as defined along the virtual crystal approximation (VCA). A random Si $\leftrightarrow$ Ge distribution was assumed. Again, changes in the bond force constants due to local bond distortions, referred to as anharmonic effects, were neglected. The vibration patterns of the modes that dominantly contribute to the minor Raman features were successively identified as 1 ( $\text{Si}_0$ ,  $\sim 385 \text{ cm}^{-1}$ ), 2<sub>1</sub> ( $\text{Si}_1$ ,  $\sim 393 \text{ cm}^{-1}$ ), 3<sub>1</sub> ( $\text{Si}_2$ ,  $\sim 427 \text{ cm}^{-1}$ ), 4<sub>1</sub> ( $\text{Si}_3$ ,  $\sim 445 \text{ cm}^{-1}$ ), 4<sub>2</sub> ( $\text{Si}_3$ ,  $\sim 459 \text{ cm}^{-1}$ ), and 5<sub>1</sub> ( $\text{Si}_4$ ,  $\sim 471 \text{ cm}^{-1}$ ). The corresponding vibration patterns are schematically reproduced in Fig. 2(b). In doing so, we preserve the original notation  $N_M$  of Grein and Cardona<sup>20</sup> for direct reference to their work. The main label indicates the number of Si atoms per Si-centered unit, the subscript referring to increasing frequencies of the distinct vibration modes originating from that unit. An important result noted by Grein and Cardona is that in many cases several modes from different units contribute to the same Raman line (refer to  $x = 0.75$  in Fig. 2(b)).

De Gironcoli (Ref. 21) reported a full *ab initio* calculation of the Raman spectra on a series of disordered SiGe alloys using large supercells (512 atoms). Almost-perfect agreement with the experiment was achieved. This correlates with an earlier conclusion of Alonso and Winer (Ref. 9) that the collection of weak Raman features is due to local fluctuations of the atomic structure in a disordered alloy. De Gironcoli and Baroni (Ref. 22) provided further insight into the origin of the minor features by focusing their attention on the disordered  $\text{Si}_{0.5}\text{Ge}_{0.5}$  alloy and by tracing the overall Raman signal into a sequence of Ge- and Si-related partial phonon density of states being due to all possible Ge- and Si-centered tetrahedron units. Interestingly, the *ab initio* calculations reveal that the Ge atoms do not vibrate in the spectral range covered by the minor features. Therefore, these are all due to Si vibrations in different local (Si,Ge)-mixed environments, as anticipated by Alonso and Winer.<sup>9</sup> De Gironcoli and Baroni (Ref. 22) found a basic correspondence between the minor features and the  $\text{Si}_n$  units that is opposite that proposed by Alonso and Winer<sup>9</sup>: the large  $n$  values referring mainly to low-frequency modes, and vice versa.

What emerges, in a nutshell, is that six oscillators [ $1 \times (\text{Ge-Ge})$ ,  $1 \times (\text{Si-Ge})$ ,  $4 \times (\text{Si-Si})$ ] would be sufficient to catch the SiGe Raman pattern at intermediate composition (ovals in Fig. 2(b)), as proposed by Alonso and Winer (Ref. 9). The high-frequency Si-Si oscillator ( $\text{Si}_4$ ) evolves into the main Si-Si feature when the Si content increases, while

the three remaining Si-Si oscillators ( $\text{Si}_{1-2-3}$ ) remain minor and exhibit little change in frequency or intensity when the alloy composition changes, as originally observed by Brya.<sup>15</sup> Grein and Cardona, on the one hand,<sup>20</sup> and de Gironcoli and Baroni, on the other,<sup>21,22</sup> developed phonon calculations at intermediate composition that have led to refinement of the assignment of Alonso and Winer<sup>9</sup> without challenging the basic picture.

Complications arise when entering the Si- and Ge-moderate/dilute limits. Recent experimental and theoretical insights, gained by Rath *et al.*<sup>16</sup> and by Franz *et al.*,<sup>17</sup> reveal unexpected trends. In particular a series of remarkable intensity interplays (RIs), hereafter referred to as  $\text{RI}_{1-2-3}$ , was detected between neighboring Raman features. These play an important role in our work.

In the Si-Si spectral range, one such RI occurs at moderate Si content between the main Si-Si mode (underscored) and the minor mode that grows on its low-frequency side (not underscored), as apparent in Fig. 1. Such interplay was briefly mentioned by Alonso and Winer<sup>9</sup> and is observable in the Raman spectra reported by Rath *et al.* (refer to the higher-frequency doublet at  $x = 0.536$ , 0.70, and 0.86 in Fig. 11 of Ref. 16). Quasiperfect intensity matching is detected around the critical Ge content  $x_{c1} \approx 0.70-0.80$  ( $\text{RI}_1$ ). This is visible in Fig. 1, as well as in the corresponding theoretical spectra reported by de Gironcoli (refer to Fig. 5 of Ref. 21). At lower Si content, the low-frequency peak becomes dominant; eventually, in the Si-dilute limit, only that mode survives, as clearly observed in the explicit data of Franz *et al.* (digitalized from Fig. 6b of Ref. 17), which are reproduced in Fig. 3(a). Based on their calculations using an anharmonic version of the Keating model and disordered large supercells (512 atoms), Franz *et al.*<sup>17</sup> assigned the low- or high-frequency components of the doublet as being due to Si-Si bond stretching, with the Si-Si bond either isolated in Ge ( $\text{Si}_1$ ) or vibrating in presence of a third Si atom ( $\text{Si}_2$ ), respectively (see Fig. 2(b)).

Somewhat surprisingly, similar scenarios develop for the main Si-Ge mode when entering the Ge- and Si-dilute limits, though within a more restricted composition domain. This is apparent in the Raman data of both Franz *et al.* (taken from Fig. 6b of Ref. 17) and Rath *et al.* (taken from Fig. 1 of Ref. 16), as reproduced in Fig. 3(b) and 3(c), respectively. In each case, the main Si-Ge mode (underscored) is progressively relayed by a minor mode that grows on its low-frequency ( $x \approx 1$ , Fig. 3(b)) or high-frequency ( $x \approx 0$ , Fig. 3(c)) side (not underscored). At a certain stage, the side mode turns dominant. Remarkably, quasiperfect intensity matching between the main and the side features is achieved at nearly symmetrical contents of the minor species at the Si-dilute ( $x_{c2} \approx 0.9$ ,  $\text{RI}_2$ , Fig. 3(b)) and Ge-dilute ( $x_{c3} \approx 0.1$ ,  $\text{RI}_3$ , Fig. 3(c)) limits. Explicit contour modeling of the Raman lineshapes in this respect are reported by Rath *et al.* (refer to Fig. 9, left, of Ref. 16, top and bottom panels).

With small Si content ( $x \approx 1$ ), abundant data indicate that, eventually, the side mode at low frequency remains alone at high Si dilution (Fig. 3(b)) before total disappearance. The side mode is thus naturally identified as Si-LVM ( $\text{Si}_0$ ). Therefore, the so-called main Si-Ge feature does not connect with the Si-LVM. This strongly reminds us of the problem faced by

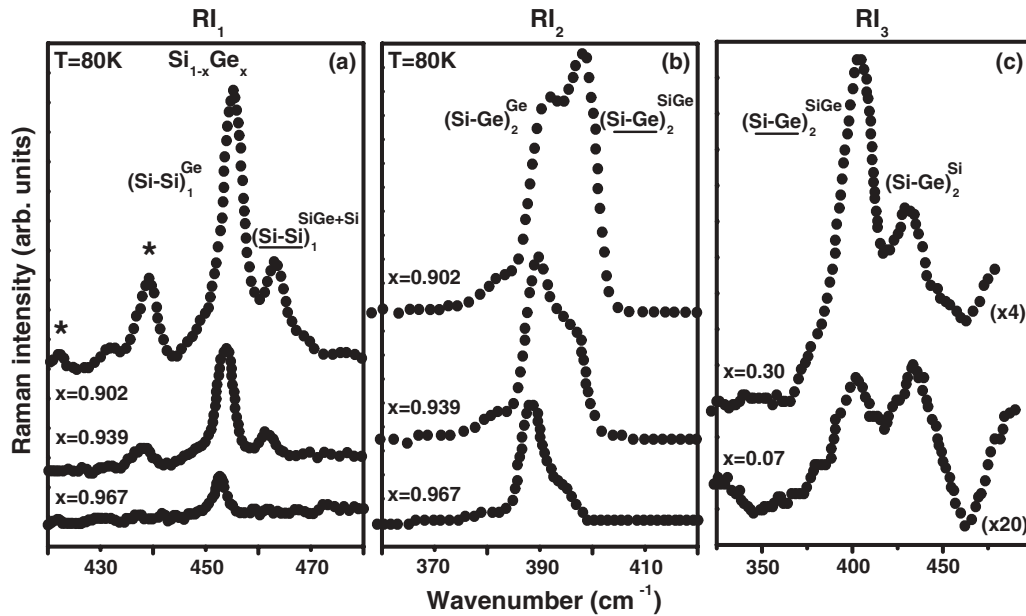


FIG. 3. RIs between the main and the minor SiGe Raman features.  $\text{Si}_{1-x}\text{Ge}_x$  Raman spectra representative of the RIs taking place between the main (underscored) and the minor (not underscored) Raman features in the (a) Si-Si ( $\text{RI}_1$ ) and (b) and (c) Si- and (c) Ge-moderate/dilute limits. The presented data in all panels were digitalized from raw experimental spectra taken by Franz *et al.* at low temperature ((a) and (b)), for better resolution of neighboring Raman features, and by Rath *et al.* (c) (i.e., from fig. 7, bottom, of Ref. 17; from fig. 1 of Ref. 16; and from fig. 6b of Ref. 17). In panel (c), the data were reproduced after proper renormalization using the original factors, as specified within parentheses. In panel (a), the asterisks refer to decomposition of the original  $(\text{Si} - \text{Ge})_2^{\text{Si}}$  band into a pseudodoublet (an overview is given in Fig. 1).

Brya in the Ge-dilute limit, in reference to the previously mentioned long-standing enigma.<sup>15</sup> A feature reminiscent of the so-called main Si-Ge feature at high frequency just before total disappearance was attributed by Franz *et al.*<sup>17</sup> to the bending mode of an isolated Si-Si pair ( $\text{Si}_1$ ). Such an assignment of the nearby  $\text{Si}_0$ - and  $\text{Si}_1$ -like features  $\sim 400 \text{ cm}^{-1}$  was already achieved by Grein and Cardona (see Fig. 2(b)); also compare Fig. 10b of Ref. 17 with Fig. 3 of Ref. 20). However, the intensity interplay between the two features was not commented on. A basic problem is that  $\text{RI}_2$  brings in an extra oscillator (outside the ovals in Fig. 2(b)) on top of the six ones already identified by Alonso and Winer,<sup>9</sup> resulting in a total of seven oscillators. Weak features were observed by Franz *et al.* on the low-frequency side of the Si-LVM in the highly dilute limits, i.e., near  $x \approx 0.99$  (see Fig. 5 of Ref. 17). However, these were attributed by Franz *et al.*<sup>17</sup> to the natural Si isotopes.

With small Ge content ( $x \approx 0$ ), the data are rather scarce. If we refer to the Raman spectrum taken by Rucker and Methfessel using the  $\text{Si}_{0.878}\text{Ge}_{0.11}\text{C}_{0.012}$  alloy with negligible C content (refer to Fig. 6 of Ref. 3), the side mode at high frequency already dominates the so-called main Si-Ge mode at  $x = 0.11$ . The trend is reinforced at  $x = 0.07$  (Fig. 3(c)). It would have been interesting to see what happens when approaching the highly Ge-dilute limit, but we are not aware of any Raman data at a lower Ge content than 7 at.%. By analogy with  $\text{RI}_2$ , we anticipate that only the side mode at high frequency will survive, eventually connecting with the Ge-LVM ( $\text{Ge}_0$ ). This would solve the long-standing enigma raised up by Brya.<sup>15</sup>

To summarize this brief overview of the literature over the last four decades, we are left with seven oscillators—not six, as is usually admitted (refer to the ovals in Fig. 2(b)). A further basic problem relates to the traditional assignment of the Si-Ge Raman signal, by searching for it, to a single Si-Ge candidate mode, which, however, falls neither to Ge-LVM ( $x \approx 0$ ) nor to Si-LVM ( $x \approx 1$ ) in corresponding dilution limits. Moreover, three interesting intensity interplays, involved with the main Si-Si and Si-Ge features in reference to  $\text{RI}_1$  and  $\text{RI}_{2-3}$ , respectively, remain unexplained. Finally, one remarkable feature arises: the critical  $x$  values for  $\text{RI}_2$  and  $\text{RI}_3$  are nearly symmetrical (corresponding to  $\sim 10$  impurity at.%), which cannot be merely fortuitous.

To our view, the latter point ( $x_{c2} \approx 1 - x_{c3}$ ), which has attracted no attention so far, appeals to strictly similar assignment of the two side features within the same global scheme. This cannot be achieved within the current six-oscillator scheme shown in Fig. 2(b), because  $\text{RI}_2$  involves a seventh oscillator. More generally, any formalization of the observed RIs seems forbidden if we start from the current 3D assignment of the individual Raman lines in terms of the  $\text{Si}_n$  and  $\text{Ge}_n$  units (Fig. 2(b)). This is because each Raman line is usually due to several units, not to a single one, as noted by Grein and Cardona.<sup>20</sup> This makes it difficult, in principle, to derive explicit laws for the composition dependence of the intensities of the individual Raman lines. Such explicit laws are still missing.

The main objective of this work is to design a simple scheme that provides a consistent assignment of the whole set of Raman lines over the composition domain and that

naturally accounts for the observed composition dependence of the intensities of various modes, in reference to  $RI_{1-2-3}$ .

To achieve this objective, we take advantage of a specificity of Raman scattering: that it operates at the BZC ( $q \approx 0$ ). Such a restriction is interesting on the theoretical side, because at this limit the space phase term ( $\vec{q} \cdot \vec{r}$ ) of the plane wave that ideally describes a phonon disappears, along with all information on the actual position ( $\vec{r}$ ) of an atom in the real (3D) crystal. Therefore, a phenomenological description of the lattice dynamics in one dimension (1D), along the so-called linear chain approximation (LCA), should, in principle, be sufficient. In this case, the Raman active mode of a pure diamond crystal, say, Si, which corresponds to out-of-phase motions of the two intercalated face-centered cubic (fcc) sublattices in the 3D diamond lattice, each being considered quasirigid ( $q \approx 0$ ), simply transposes at 1D into Si-Si bond stretching. Generalizing to the SiGe alloy, this means that the related Raman lines should be discussed in terms of Ge-Ge, Si-Ge, and Si-Si bond stretching at 1D. The same bond may give rise to distinct Raman features, which comes to distinguish among various local LCA-type (1D) environments of that bond. Such a 3D $\rightarrow$ 1D change of scope for the basic understanding of the 1-bond  $\rightarrow$  multimode SiGe Raman pattern remains unexplored.

Three phenomenological, i.e., LCA-based (1D), schemes are available in the literature for the description of the Raman spectra of alloys, as originally worked out for  $A_{1-x}B_xC$  zincblende crystals ( $C$  denoting indifferently a cation or an anion). The first two, i.e., the modified random-element isodisplacement (MREI, Ref. 26) and cluster (Ref. 27) schemes, were developed at the emergence of such alloys in the mid-1960s. In the MREI scheme the bonds of a given species, i.e.,  $AC$ - or  $BC$ -like, are all supposed to contribute to the same unique Raman line at a given alloy composition (1 bond  $\rightarrow$  1 mode), irrespective of their local environment. In contrast, the cluster scheme distinguishes among like bonds depending on their first-neighbor environment at 3D out of four possible clusters in a zincblende alloy (1 bond  $\rightarrow$  4 modes). In each case, the equivalence between like elementary oscillators at a given alloy composition, i.e., the chemical bond in the MREI scheme and the chemical bond in its first-neighbor sphere in the cluster scheme, is formalized by considering that such oscillators are immersed into the same uniform VCA-type continuum. This provides smooth composition dependence of the phonon frequencies by construction. As for the intensity of a given Raman line, this simply scales as the fraction of corresponding elementary oscillator in the crystal. The remaining scheme, i.e., the so-called percolation scheme,<sup>28</sup> introduces a description of a random  $A_{1-x}B_xC$  alloy in terms of a composite of the  $AC$ - and  $BC$ -like host regions, not in terms of a uniform VCA-type continuum as with the MREI and cluster schemes. This naturally leads to distinguish among vibrations of like bonds depending on two environments (1 bond  $\rightarrow$  2 modes). Schematic comparisons between the contents of the cluster and MREI schemes, on the one hand, and of the percolation scheme, on the other hand, are available, e.g., in Figs. 1 of Refs. 28 and 29, respectively. Persistent shortcomings in the current version of the percolation scheme are concerned with the nature of the  $AC$ - and  $BC$ -like host regions, regarding both the composition and the length scale.

As far as SiGe is concerned, the 1-bond  $\rightarrow$  1-mode MREI scheme is clearly undersized in view of the natural complexity of the Raman spectra. Besides, some of us have shown that the 1-bond  $\rightarrow$  4-mode cluster scheme is not devoid of conceptual ambiguities and seems thus misleading regarding the nature of the alloy disorder.<sup>30</sup> What remains is the percolation scheme. The second objective of this work is to see whether the percolation scheme, successfully used for  $A_{1-x}B_xC$  zincblende alloys,<sup>28,29</sup> may further apply to the diamond-type  $Si_{1-x}Ge_x$  alloy.

In an attempt to extend the percolation scheme to SiGe, we are aware that certain adaptation might be needed with respect to the original 1-bond  $\rightarrow$  2-mode version because of the zincblende  $\rightarrow$  diamond change in the crystal structure. Moreover, the number of bond species enlarges from two in a ternary  $A_{1-x}B_xC$  zincblende alloy ( $A$ - $C$  and  $B$ - $C$ ) to three in the binary  $Si_{1-x}Ge_x$  diamond alloy (Ge-Ge, Si-Ge, and Si-Si). This is because all sites are likely to be occupied by the two-atom species in  $Si_{1-x}Ge_x$ , while the  $C$  sublattice remains unperturbed in  $A_{1-x}B_xC$  zincblende alloys. Additional complications might arise in that the dispersion of the optical phonon is dramatically large in the pure Si and Ge crystals, i.e., on the order of several tens of reciprocal centimeters,<sup>31</sup> while it is almost negligible for the parents of all re-examined zincblende alloys so far, i.e., usually less than several reciprocal centimeters.<sup>28</sup> Finally, we anticipate, in view of the unusually high complexity of the SiGe Raman spectra, that the percolation scheme may not be adaptable to SiGe as long as the percolation-type environments of a bond remain undetermined at the microscopic scale (explained earlier). In view of such positioning of SiGe with respect to  $A_{1-x}B_xC$  zincblende alloys, we feel it is useful, at any stage of the development of the SiGe version of the percolation scheme, to establish a comprehensive comparison with the original and well-established version for  $A_{1-x}B_xC$  zincblende alloys for reference purpose.

The manuscript is organized as follows. In Sec. II, we introduce an improved version of the percolation scheme for the reference  $A_{1-x}B_xC$  zincblende alloys, in which the existing shortcomings regarding the exact nature of the  $AC$ - and  $BC$ -like environments of a bond are overcome. Based on this, we design in Sec. III A a seven-oscillator [ $1 \times$  (Ge-Ge),  $4 \times$  (Si-Ge),  $2 \times$  (Si-Si)] version of the percolation scheme for random  $Si_{1-x}Ge_x$  that naturally accounts for all observed intensity interplays ( $RI_{1-2-3}$ ). This deviates considerably from the prevalent six-oscillator [ $1 \times$  (Ge-Ge),  $1 \times$  (Si-Ge),  $4 \times$  (Si-Si)] picture reported in Fig. 2(b) (refer to the ovals). The percolation-type reassignment of the individual Raman lines realized in Sec. III A, based on the composition dependence of their intensities, is independently secured in Sec. III B, via an *ab initio* insight into the frequencies of bond-stretching modes along selected 3D-impurity motifs. These are taken as pseudolinear so as to remain in the spirit of the LCA, upon which the percolation scheme relies. In Sec. III C, we give an overview of the SiGe percolation-type Raman lineshapes over the composition domain, after *ab initio* calibration of the Ge-Ge, Si-Ge, and Si-Si Raman efficiencies. In Sec. IV, we compare the SiGe and zincblende versions of the percolation scheme. A natural zincblende reference is GaAsP due to its lattice mismatch similar to that in SiGe. A striking difference

between the two schemes is an inversion of the order of the like phonon modes in the Si-Si (Sec. IV A) and Si-Ge (Sec. IV B) multiplets with respect to the well-resolved Ga-P doublet. Such inversions are discussed via a comparative *ab initio* insight into the bond lengths and BZC phonons of prototype impurity motifs that are directly transposable to the two crystal structures. Conclusions are summarized in Sec. V.

## II. MODIFIED VERSION OF THE PERCOLATION SCHEME FOR THE REFERENCE ZINCBLENDE ALLOYS

Our aim in this section is to identify the microstructure of the *AC*- and *BC*-like percolation-type environments of a bond in the reference  $A_{1-x}B_xC$  zincblende alloys, in terms of composition and length scale. In doing so we focus on the non-polar transverse optical (TO) modes of such alloys, which assimilate in nature with the optical modes of SiGe.

### A. Raman intensity aspect

The intensity of a given Raman mode is monitored by its oscillator strength. In the current version of the percolation scheme, the available oscillator strength per bond, which scales as the corresponding bond fraction, divides between the two like modes of a given percolation doublet in proportion of the scattering volumes of the *AC*- and *BC*-like host regions. These are simply assumed to scale as the related bond fractions. Accordingly the intensities of the two like Raman features that form the *AC*- and *BC*-like percolation doublet, referring to *A-C* and *B-C* vibrations in the *AC*- and *BC*-like environments, respectively, scale as follows:  $(1-x)^2$  and  $(1-x) \cdot x$  for *A-C* and *B-C* vibrations, respectively, in *AC*-like environments and  $x \cdot (1-x)$  and  $x^2$  for *A-C* and *B-C* vibrations, respectively, in *BC*-like environments. The two like modes from the same doublet thus have similar intensities near  $x \approx 0.5$ , and the dominant mode at one end of the composition domain ( $x \approx 0,1$ ) turns minor at the other end. Such RI was unambiguously observed with the Raman signal of the short Be-based bond of both ZnBeSe<sup>32,33</sup> and ZnBeTe<sup>34</sup> alloys.

In our search to identify the microstructure (composition and length scale) of the *AC*- and *BC*-like environments, we face a double constraint. First, regarding the length scale, it is remarkable that most phonon dispersion curves of a pure crystal, e.g., Ge or Si, can be reproduced by considering central and noncentral interatomic force constants between first neighbors only.<sup>35</sup> Accordingly, any assignment of the *AC*- and *BC*-like environments in the alloy beyond the second or third neighbors of a bond might not be realistic. Second, such environments should be defined at 1D, not at 3D as in the cluster model. This is to remain consistent with the LCA upon which the percolation scheme relies.

The previously mentioned scaling of the Raman intensities on the alloy composition is preserved simply by considering that the percolation model distinguishes between the stretching of a bond depending on its *AC*- or *BC*-like first-neighbor environment at 1D. For example,  $C(AC)B$  is identified as the 1D oscillator for the *A-C* bond stretching in the *BC*-like environment. The corresponding fraction of oscillator then expresses as the probability of finding *B* ( $x$ ) next to *A*

$(1-x)$  on the 1D (*A,B*)-like substituting sublattice, the two probabilities being independent in case of random  $A \leftrightarrow B$  substitution. The 1D oscillators for *A-C* bond stretching in the *AC*-like environment and for *B-C* bond stretching in the *AC*- and *BC*-like environments are likewise identified as  $C(AC)A$ ,  $C(BC)A$ , and  $C(BC)B$ , respectively.

### B. Raman frequency aspect

The two possible *AC*- and *BC*-like environments of a bond undergo a major transition when the alloy composition changes. This concerns their spatial organization in the crystal. Such a transition occurs at the so-called *A-C* and *B-C* bond percolation thresholds (BPT's). The BPT's correspond to critical alloy compositions at which the bond species that form the minor environment, i.e., the *A-C* ones with small *A* content and the *B-C* ones with small *B* content, connect spontaneously into a pseudoinfinite treelike continuum spreading throughout the crystal.<sup>36</sup> This is a pure statistical effect of the random substitution on the (*A,B*) sublattice.<sup>36</sup> Below the BPT the minor bonds are only connected into finite treelike chains, with dispersion in size. In a random  $A_{1-x}B_xC$  zincblende alloy, the *B-C* BPT is identified near  $x_B \approx 0.19$ , while the symmetrical composition  $x_A \approx 0.81$  refers to the *A-C* BPT.<sup>36</sup> The crucial point is that the internal structure of the treelike chains of a given type, i.e., *AC*- or *BC*-like, drastically changes when turning from finite to infinite, as detailed later. Because the phonon frequency depends on the local environment, this gives rise to a percolation-type singularity in the frequency of the stretching modes of the hosted bonds.

We focus on the *BC*-like 1D environment for clarity. A key result of the percolation site theory is that the *BC*-like treelike continuum that forms right at the BPT ( $x = x_B$ ) is a pure fractal. This means that if we take a given *B* atom from this pseudoinfinite cluster and put it at the center of an imaginary cube with variable edge *L*, then the fraction of the cube occupied by the *B* atoms from the pseudoinfinite cluster decreases regularly according to a scaling law with a stable exponent smaller than the dimension of the lattice, i.e., three in the present case, when *L* increases (see Ref. 36, chapter 3). This introduces a basic notion behind the concept of fractal: the arrangement of the *B* atoms forming the pseudoinfinite continuum is self-similar, i.e., stable, at all scales.<sup>36</sup>

Now, consider what happens on each side of a BPT. Another key result of the percolation site theory is that as soon as the alloy composition has departed from the BPT, the fractal character is lost.<sup>36</sup> Below the *B-C* BPT ( $x < x_B$ ), where the *BC*-like region merely consists of a dispersion of finite clusters with different sizes, the fractal behavior somehow survives; however, some deviation with the original scaling law (explained earlier) should be taken into account, and the deviation increases when the size of the finite clusters decreases.<sup>36</sup> Nevertheless, in such a regime, which we refer to as "fractal-like," the local environment of the *A-C* and *B-C* bonds vibrating within the fine-size *BC*-like clusters remains quasistable, i.e., quasi-independent on the alloy composition  $x$ ,<sup>36</sup> leading to quasi-invariance of the corresponding TO frequencies ( $0 < x < x_B$ ). In contrast, above the *B-C* BPT ( $x > x_B$ ), the *BC*-like continuum that results from the coalescence of the finite-size clusters enters a so-called normal

regime. This means that, at a given alloy composition, the fraction of the previously mentioned cube that is occupied by the  $B$  atoms from the pseudoinfinite cluster basically scales as the volume  $L^3$  of the cube, just as for a homogeneous object, justifying the terminology “normal behavior”. Accordingly, in the percolation scheme, we assimilate the  $BC$ -like continuum ( $x > x_B$ ) with a submesoscopic alloy within the main macroscopic  $A_{1-x}B_xC$  alloy by using a renormalized MREI description. In this description, the  $BC$ -like continuum takes a pseudoalloy composition  $y$  that is linearly rescaled with respect to the actual alloy composition  $x$ . It varies between 0 and 1 when  $x$  varies between the pure  $BC$ -like fractal ( $x = x_B$ ), taken as a pseudoparent ( $y = 0$ ) and the pure  $BC$  crystal ( $x = y = 1$ ).<sup>32</sup> A smooth  $x$  variation generates in turn a smooth  $y$  variation, with concomitant impact on the TO frequencies of the  $A-C$  and  $B-C$  bonds vibrating in the  $BC$ -like suballoy ( $x_B \leq x \leq 1$ ).

We admit that the previously mentioned spectacular change in the nature of the composition dependence of the TO frequencies on each side of the BPT (i.e., from quasistable in the dispersion regime, referred to as quasifractal, to smoothly  $x$  dependent in the continuum regime, referred to as normal) could so far be observed only with the ZnBeSe<sup>32,33</sup> and ZnBeTe<sup>34</sup> alloys that exhibit a unusually large contrast in their bond physical properties (Ref. 37). For less contrasted alloys, the percolation-type singularities in the Raman frequencies do not show up that evidently.<sup>28,29</sup> Such singularities are the only justification for the terminology of a percolation scheme. If they cannot be detected, we may as well abandon the Raman frequency aspect<sup>38</sup> and replace the terminology of a percolation scheme with that of a 1D-cluster scheme (by opposition with the 3D-cluster scheme of Verleur and Barker, Ref. 28), in reference to the Raman intensity aspect only (see Sec. II A).

### C. *Ab initio* protocol

We must verify that the novel 1D assignment of the  $AC$ - and  $BC$ -like environments of a bond (see Sec. II A) is technically consistent with our simple *ab initio* protocol used to access the two input parameters as needed per bond to implement the 1D-cluster/percolation scheme, i.e., the frequency of the impurity mode  $\omega_{imp}$ , plus the splitting  $\Delta$  between the like TO modes of the same percolation doublet.<sup>29</sup>

We consider the  $BC$ -like percolation doublet. To determine  $\omega_{imp}$ , we use a large  $AC$ -like supercell containing a unique  $B$  impurity. This is the ultimate configuration that refers to an impurity ( $B$ ) vibrating in the environment of the other species ( $AC$ -like). We then search for the vibration frequency of that impurity. There is only one triply degenerate (triplet) mode for the isolated  $B$  atom. At 1D, this naturally identifies with the  $C(BC)A$  oscillator. To determine  $\Delta$ , we consider a pair of  $B$  impurities sitting nearby on the  $fcc$  substituting sublattice, forming a  $B-C-B$  pseudolinear chain. This is the ultimate configuration that refers to an impurity ( $B$ ) vibrating in its own environment ( $BC$ -like). The vibration pattern of the  $B-C-B$  pseudolinear chain divides into two distinct series of BZC-like modes. The first series reduces to a singlet, corresponding to in-phase motion of the  $B$  atoms along the axis of the chain, against the intermediary  $C$  atom ( $q \approx 0$ ). Basically, this refers

to  $B-C$  bond stretching along the pseudolinear  $B-C-B$  chain, thus identified with  $C(BC)B$  at 1D. The second series consists of a multiplet including all possible bending modes of the  $B-C-B$  chain near  $q \approx 0$  in their in-plane and out-of-plane variants. Such bending modes of the  $BC$ -like chain correspond to  $B-C$  bond-stretching perpendicular to the chain, i.e., inside the surrounding  $AC$ -like environment. As such, they identify with the  $C(BC)A$  oscillator at 1D. We checked that the bending modes of the  $B-C-B$  chain emerge close to  $\omega_{imp}$ . (e.g., Fig. 3 in Ref. 28).  $\Delta$  is then estimated as the frequency gap between the  $C(BC)A$  impurity mode and the  $C(BC)B$  mode from the pair.

Incidentally, we checked that a pseudolinear continuum of  $B-C$  bonds, i.e., the natural percolation-type motif for  $B-C$  bonds vibrating in a  $BC$ -like environment, provides a Raman pattern similar to that for the finite  $B-C-B$  chain mentioned previously (compare the spectra in Figs. 9 and 3 of Refs. 39 and 40, respectively). In practice, the *ab initio* protocol is thus operated using the latter, simpler motif.

The reactualized version of the percolation scheme is not a predictive one but instead offers a versatile framework for the interpretation of any 1-bond  $\rightarrow$  multimode Raman pattern of any alloy. The 1D oscillators can be expanded at will, in principle, depending on the number of observed Raman lines per bond and on the observed composition dependence of the Raman intensities. Such flexibility is crucial in our interpretation of the SiGe Raman spectra, as shown later.

## III. PERCOLATION SCHEME FOR RANDOM SIGE

In our review of the SiGe Raman spectra, we did not find any hint of singularity in the composition dependence of the Raman frequencies at any BPT.<sup>41</sup> This is not surprising because of the rather small contrast in the bond physical properties of the Si and Ge crystals (see Sec. I). This also means that understanding of such curves falls beyond the scope of our simple percolation scheme. Thus, in our work, we emphasize the Raman intensity aspect and adopt, from now on, the terminology of a 1D-cluster scheme for SiGe (see Sec. II B).

### A. 1D-cluster assignment of the individual Raman lines: An intensity-based approach

In practice, we proceed as follows for the reassignment of the SiGe Raman pattern at 1D.

First, we investigate roughly which Raman lines refer to which bond species. This is already known for the three main Raman features (see minor panels in Fig. 1), which are thus used as references. The assignment of the remaining four minor features is then inferred from the subtle inversions of dominance observed between the main or reference features (underscored in Figs. 1 and 3) and the minor or unknown ones (not underscored), in reference to  $RI_{1-2-3}$ . The basic idea is that the features involved in such interplays are coupled in some way and hence basically relate to the same bond stretching. Accordingly, the low-frequency feature that counterbalances the main Si-Si one in  $RI_1$  (near  $x_{c1} \approx 0.70$ , Fig. 3(a)) and the two satellite ones challenging the main Si-Ge feature in  $RI_{2-3}$  (near  $x_{c2} \approx 0.9$  and  $x_{c3} \approx 0.1$ , Fig. 3(b))

and 3(c), respectively) would relate to Si-Si and Si-Ge bond stretching, respectively. In this case, the Si-Si doublet and the Si-Ge triplet indicate that the corresponding bond stretching distinguishes between two and three types of 1D environments, respectively. Only three RIs are identified for four minor modes. One minor mode should thus remain unassigned, the one corresponding to the dotted line in Fig. 2. More detail is given later.

The next issue is to identify the microstructure of the distinct 1D environments per Si-Si and Si-Ge bond in terms of both length scale and composition. We use two criteria: (1) simplicity, in view of BZC phonons essentially proceeding from short-range interactions (see Sec. II A), and (2) an ability, behind the corresponding fractions of elementary “bond + environment” 1D oscillators (as estimated on the basis of random Si↔Ge substitution), to reproduce the corresponding RIs at the observed alloy compositions, i.e., at  $x_{c1}$  for the Si-Si doublet (RI<sub>1</sub>) and at the symmetrical  $x_{c2}$  and  $x_{c3}$  values for the Si-Ge triplet (RI<sub>2</sub> and RI<sub>3</sub>, respectively).

### 1. Si-Si spectral range

First, we consider the Si-Si doublet. At the Si-dilute limit, most Si-Si bonds are isolated in the Ge-like matrix. Only a small fraction of these are sitting near other Si impurities. The trend is progressively reversed when increasing the Si content until at a certain stage, the second environment becomes dominant.<sup>36</sup> Our view is that RI<sub>1</sub> simply reflects such an inversion of population. This naturally leads to a crude assignment of the low- and high-frequency components of the Si-Si doublet as resulting from Si-Si bond stretching in Ge- and Si-like environments, respectively.

For deeper insight, we investigate whether it is possible to define such 1D environments at the minimum length scale of first neighbors, in reference to criterion 1. There are three possible Si-Si oscillators then: Si(SiSi)Si, Si(SiSi)Ge, and Ge(SiSi)Ge, corresponding to Si-Si bond stretching in pure-Si, (Si,Ge)-mixed, and pure-Ge 1D environments, respectively. The fractions of such “bond + environment” 1D oscillators simply express by weighting the Si-Si bond fraction (in reference to the atom species within the brackets), i.e.,  $(1-x)^2$ , by the corresponding fractions of 1D environments (in reference to the atom species outside the brackets), i.e.,  $(1-x)^2$ ,  $2x \cdot (1-x)$ , and  $x^2$ , assuming a random Si↔Ge substitution. If we assume further that the Raman polarizability of the Si-Si bond does not depend on its local neighborhood, in a first approximation,<sup>42</sup> then quasiperfect intensity matching at  $x_{c1}$  (cf. RI<sub>1</sub>), in reference to criterion 2, is achieved simply by assigning the low- and high-frequency Raman lines of the Si-Si doublet to the individual Ge(SiSi)Ge oscillator and to the couple of [Si(SiSi)Ge, Si(SiSi)Si] oscillators taken as indiscernible, respectively. Perfect intensity matching is then expected at 70 at.% Ge. This is consistent with experimental findings (refer to the Si-Si doublet at  $x = 0.77$  in Fig. 1), especially those of Rath *et al.* (refer to the morphological changes within the broad Si-Si band in Fig. 11 of Ref. 16), and with theoretical ones (in reference to the bottom panel of Fig. 5 in Ref. 21). Accordingly, Si-Si bond stretching distinguishes between full-Ge and alternative first-neighbor 1D environments. The corresponding modes are labeled

hereafter as  $(\text{Si} - \text{Si})_1^{\text{Ge}}$  and  $(\text{Si} - \text{Si})_1^{\text{SiGe+Si}}$ . In this compact notation, introduced from Fig. 1, the main label specifies the nature of the bond stretching, while the subscript and the superscript refer to the length scale and the composition of the 1D environment, respectively.

### 2. Si-Ge spectral range

We proceed in the same way for the Si-Ge triplet. To our view, the striking similarity between the scenarios that develops for the main Si-Ge feature when entering the Si- and Ge-moderate/dilute limits implies assignments that are strictly similar in nature for the two Si-Ge side features involved in RI<sub>2-3</sub>. In Fig. 3(b) and 3(c), the two side features (not underscored) dominate the main one (underscored) in the Ge- and Si-dilute limits, where the environments of any Si-Ge bond are dominantly of the Si and Ge types, respectively. The corresponding side features are thus attributed to Si-Ge bond stretching in Ge- and Si-like environments, respectively. This is consistent with our basic view that the Si-Ge side features, not the main one, should connect to the Ge ( $x \approx 0$ ) and Si ( $x \approx 1$ ) LVMs (see Sec. I), thus resolving the long-standing enigma pointed out by Brya.<sup>15</sup>

Based on criterion 1, we consider first the possibility that Si-Ge bond stretching might distinguish among its three possible first-neighbor environments in 1D, as was the case for Si-Si bond stretching. The 1D oscillators associated with the top, intermediate, and bottom Si-Ge branches, mostly apparent at moderate/dilute Ge, intermediate composition, and moderate/dilute Si, would then be identified as Ge(GeSi)Ge, Si(GeSi)Ge, and Si(GeSi)Si, respectively. However, coming to criterion 2, no opportunity exists, with the corresponding fractions of oscillators, to achieve intensity matching at the observed  $x_{c2}$  (RI<sub>2</sub>) and  $x_{c3}$  (RI<sub>3</sub>) values. Intensity matching would occur at 33 at.% of the minor species, not  $\sim 10$  at.%, in contradiction with experimental findings. We thus push the assignment to second neighbors, keeping in mind that the Ge- and Si-like 1D environments should be identical in nature. In reference to criterion 2, intensity matching at  $x_{c2}$  and  $x_{c3}$  is then achieved simply by considering that the top, intermediate, and bottom Si-Ge branches distinguish among full-Si, all possible (Si,Ge)-mixed variants, and full-Ge 1D environments, respectively. Accordingly, in the case of random Si↔Ge substitution, the related fractions of oscillators are expressed as  $[2 \cdot x \cdot (1-x)^5, 2 \cdot x \cdot (1-x) \cdot \{[x + (1-x)]^4 - [x^4 + (1-x)^4]\}, 2 \cdot (1-x) \cdot x^5]$ , corresponding to intensity matching between the central and the peripheral features when entering the last 16 at.% of the composition domain. This is consistent with the data reported in Fig. 2(a) and 2(b) and with the experimental findings of Rath *et al.* (ideally corresponding to  $x_{c2} \approx 0.86$  and  $x_{c3} \approx 0.14$ , as apparent in their detailed contour modeling of the Si-Ge Raman signals using Lorentzian functions in Fig. 9(1) and 9(3) of Ref. 16, respectively). The corresponding series of 1D oscillators are written as [SiSi(GeSi)SiSi, GeSi(GeSi)SiSi + . . . + GeGe(GeSi)SiSi + . . . + GeGe(GeSi)GeSi, GeGe(GeSi)GeGe] with extended notation or  $[(\text{Si} - \text{Ge})_2^{\text{Si}}, (\text{Si} - \text{Ge})_2^{\text{SiGe}}, (\text{Si} - \text{Ge})_2^{\text{Ge}}]$  with compact notation (see Fig. 1).

We turn to the last minor oscillator, which remains unassigned (refer to the dotted line in Fig. 2). It was detected

theoretically by de Gironcoli from  $x = 0.28$  (Fig. 2(a)),<sup>21</sup> emerging at intermediary frequency between the Si-Si and the Si-Ge spectral ranges. We may thus hesitate *a priori* to assign this mode in terms of Si-Si stretching or Si-Ge stretching. The first option would be to consider that Si-Si bond stretching is sensitive to its local environment at a length scale beyond first neighbors, in contradiction to our previous explanation of RI<sub>1</sub>. Our preliminary attempts to explain RI<sub>1</sub>, along with the overall composition dependence of the unassigned minor oscillator, presuming the latter is of the Si-Si type, remained unsuccessful. Our present view is that the unassigned minor oscillator relates to the top  $(\text{Si} - \text{Ge})_2^{\text{Ge}}$  branch. Basically, soon after departing the Ge-dilute/moderate limit, this branch would split into a sort of pseudodoublet; the corresponding features are highlighted by asterisks in Figs. 1 and 3(a). Such decomposition does not challenge RI<sub>3</sub>, because it occurs afterward ( $x_{c3} < 0.28$ ). Within the scope of the 1D-cluster scheme, such decomposition would reveal that the Si-Ge bonds vibrating in the Si-like environment turn sensitive to their 1D environment at a length scale beyond second neighbors. However, we are unable to assign the actual microstructure or the length scale of such a 1D environment. This is because the intensity interplay between the two components of the pseudodoublet is obscured by the side  $(\text{Si} - \text{Ge})_2^{\text{SiGe}}$  and  $(\text{Si} - \text{Si})_1^{\text{Ge}}$  features that become strong starting with moderate Ge content. The low-frequency component is weaker than its high-frequency counterpart with large Si content (compare the intensity of the two features highlighted by asterisks in the top spectrum of Fig. 1). Such intensity interplay suggests that the two components may refer to Ge- and Si-like 1D environments, respectively, with the latter 1D environments remaining full-Si-like up to second neighbors, in reference to the native  $(\text{Si} - \text{Ge})_2^{\text{Ge}}$  mode.

### 3. 1D-cluster SiGe scheme

The resulting 1D-cluster scheme for SiGe is displayed in Fig. 4. The dotted line manifests the decomposition of the  $(\text{Si} - \text{Ge})_2^{\text{SiGe}}$  branch into the previously mentioned pseudodoublet away from the Ge-dilute limit (refer to the oval on the left-hand side of Fig. 4). Otherwise, each individual branch is ideally represented by a straight solid line, the slope being defined so as to best adjust the experimental frequencies (see Fig. 2(a)). A significant deviation with respect to linearity is only observed for the central Si-Ge branch at moderate Ge content (see Sec. III C).

Altogether the SiGe 1D-cluster scheme shown in Fig. 4 provides a description of the Raman pattern of a random SiGe alloy in terms of seven modes [ $1 \times (\text{Ge-Ge})$ ,  $4 \times (\text{Si-Ge})$ ,  $2 \times (\text{Si-Si})$ ], as covered by six generic 1D oscillators (refer to letters a–f in the figure image). This considerably deviates from the currently admitted six-oscillator [ $1 \times (\text{Ge-Ge})$ ,  $1 \times (\text{Si-Ge})$ ,  $4 \times (\text{Si-Si})$ ] picture at 3D reported in Fig. 2(b), in which the  $(\text{Si} - \text{Ge})_2^{\text{Ge}}$  oscillator is omitted. In particular, the 3D→1D reassignment is apparent in the way the like oscillators are regrouped, as schematically indicated by ovals in the two figures. The gain behind such 3D→1D reassignment is that the 1D-cluster scheme is explicit regarding the intensity aspect, apart from the presumed

decomposition of the  $(\text{Si} - \text{Ge})_2^{\text{Si}}$  branch. This applies in particular to RI<sub>1–2–3</sub> (rectangles in Fig. 4). The intensity information is made apparent via appropriate thickening of the individual branches in Fig. 4, in accordance with the individual fractions of oscillators as specified on top of each branch. The corresponding information in Fig. 2(b) is restricted to the three main Ge-Ge, Si-Ge, and Si-Si branches and is notably different with respect to Fig. 4, at least regarding the latter two branches.

### B. *Ab initio* insight at dilution limit phonon frequencies ( $x \approx 0, 1$ )

Independent insight into the 1D-cluster reassignment of the phonon branches is gained by *ab initio* phonon calculations using prototype impurity motifs taken as representative of the considered branches in their dilute limits ( $x \approx 0, 1$ ), realized by large (64-atom) supercells including one or two impurities (gray/red online triangles in Figs. 2(a) and 4). The impurity motifs are taken to be as simple as possible, with any impurity atom staying within the second-neighbor sphere of any other impurity atom from the same motif and each motif remaining beyond the second-neighbor sphere of the like motif from the next supercell. Altogether, this ensures that our supercells are sufficiently converged in size to mimic the phonon behavior of the motif as immersed into the infinite crystal.<sup>43</sup> Whenever the considered impurity motif does not merely reduce to an isolated impurity, it is designed as a pseudolinear chain (LCA type), and we focus on the bond-stretching mode along the chain ( $\parallel$  chain) for consistency with the LCA upon which the 1D-cluster model relies (see Sec. II). Such impurity motifs provide not only a  $\parallel$  chain mode but also  $\perp$  chain ones (referring to atom displacements perpendicular to the chain), with in-plane and out-of-plane variants. Nevertheless, we checked that the frequencies of the  $\perp$  chain modes related to a given LCA-type motif roughly replicate, within less than  $7 \text{ cm}^{-1}$ , the frequency of the  $\parallel$  chain mode of another such motif.<sup>44</sup> With this, no vibration mode of any motif is left unassigned, in principle. The assignment of a given 1D-cluster branch is eventually validated by a convergence of that branch onto the frequency of the  $\parallel$  chain mode of the related LCA-type motif. Such modes, as sketched out on each side of Fig. 4, are labeled by adding a subscript (0 or 1, in reference to the  $x$  value) to the letter (a–f) representing each branch.

The phonon calculations are done after full relaxation of the supercells, i.e., of the lattice constant and of the atom positions, along the procedure detailed (e.g., in Ref. 28, using more specifically Eq. (2) therein). We use density functional theory and local density approximation through the Ceperley-Alder<sup>45</sup> functional for the exchange-correlation energy in the SIESTA code (Ref. 46). We take the separable Troullier-Martins<sup>47</sup> norm-conserving pseudopotentials with a basis set generalized to include double-zeta with polarization orbitals. The cutoff energy and  $k$ -grid cutoff are 360 Ry and  $10 \text{ \AA}$ , respectively. When tested with the pure Si and Ge crystals, the obtained values of bond length, bulk modulus, and BZC-phonon frequency with the SIESTA code compare fairly well with the experimental data and with earlier *ab initio* values given by the AIMPRO code, as shown in Table I. Details regarding the AIMPRO code are given in the next subsection.

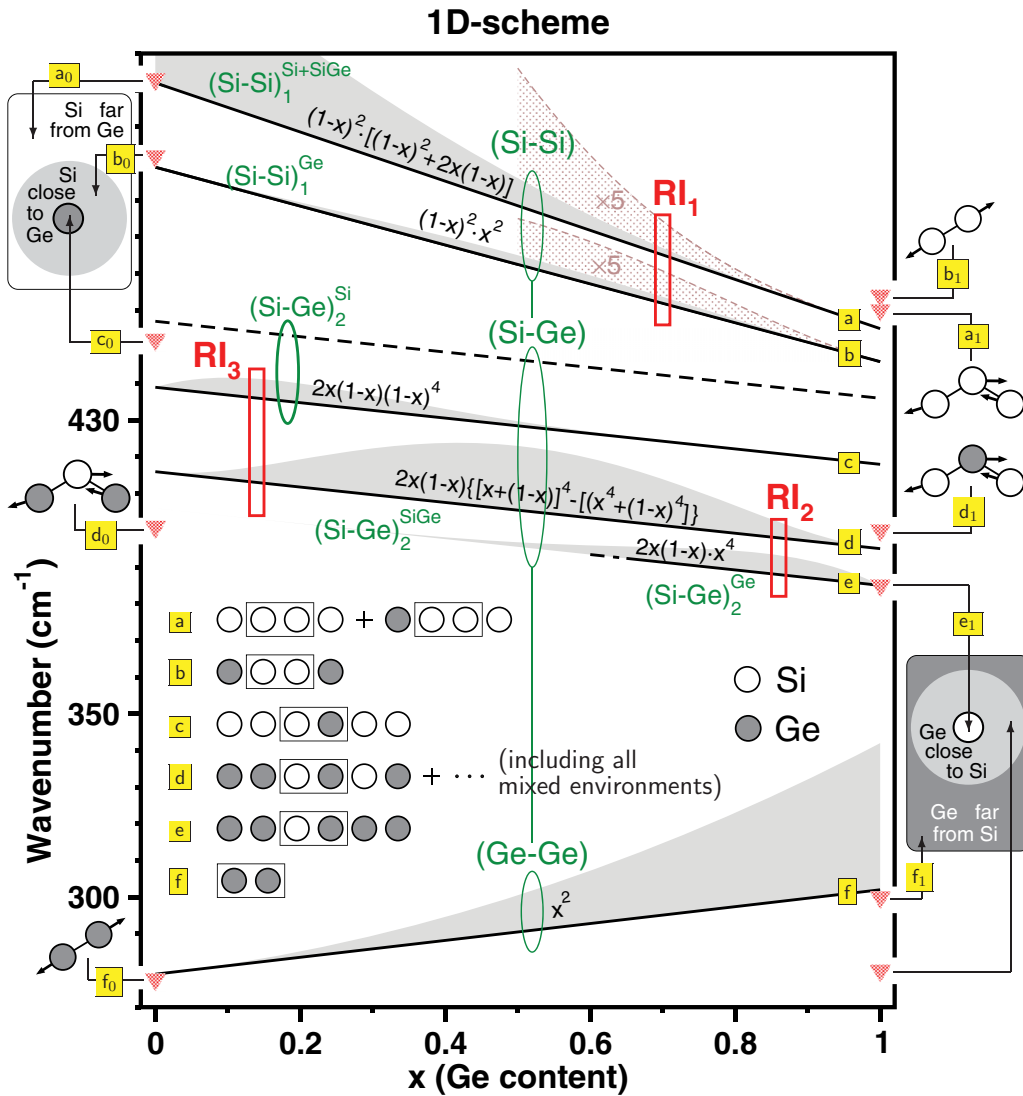


FIG. 4. (Color online) 1D-cluster scheme for random SiGe. This supports a seven-oscillator [1 × (Ge-Ge), 4 × (Si-Ge), 2 × (Si-Si)] Raman pattern for Si<sub>1-x</sub>Ge<sub>x</sub>. The individual 1D oscillators, identified as letters (a, b, etc.) are schematically represented in the body of the figure, using the same symbolic notation as in the minor panels of Fig. 1 for a direct comparison. The like phonon branches, referring to the same ultimate bond stretching (as emphasized in the symbolic notation of each oscillator), are regrouped by ovals. Altogether, the resulting 1D assignment considerably deviates from the current 3D one, as summarized in Fig. 2(b), in both the nature and the number of oscillators. When available, the individual fractions of oscillators, which monitor the Raman intensities (see text), are specified on top of each relevant branch and visualized via appropriate thickening of such branches (gray area), using the same scale as in Fig. 2(b), for a direct comparison. The overall 1D assignment, based on RI<sub>1-2-3</sub> (see rectangles) at the theoretical critical Ge contents ( $x_{c1} = 0.70$ ,  $x_{c2} = 0.86$ , and  $x_{c3} = 0.14$ ) between like Raman features (as regrouped by the same oval), is independently validated by a direct *ab initio* insight into the frequencies of prototype vibration modes (identified by a letter, in reference to the considered oscillator, plus a subscript, in reference to the  $x$  value), as indicated on each side of the figure. In the two represented supercells, containing a unique impurity atom, a simple color code is used for Si (white) and Ge (dark gray) and to materialize the impurity-induced strain in the host medium (light gray). The  $(\text{Si} - \text{Ge})_2^{\text{Si}}$  mode (refer to the oval on the left-hand side) decomposes into a distinct doublet away from the Ge-dilute/moderate limit (the two components of the doublet are identified by asterisks in Fig. 1), which is taken into account by the adjunction of a dashed line.

1. Si-Si spectral range

The 1-bond → 2-mode Si-Si doublet requires an *ab initio* insight into four limit frequencies. For the top  $(\text{Si} - \text{Si})_1^{\text{SiGe+Si}}$  branch, referring to Si-Si stretching in an undetermined SiGe- or Si-like environment, we consider two limit supercells, i.e., a pure-Si one, providing the bulk Si frequency ( $x \approx 0$ , mode  $a_0$ , 522 cm<sup>-1</sup>), plus a Ge-like one containing three quasialigned Si impurities, searching then for Si-Si stretching along the

Si-Si-Si chain. This refers to Si-Si stretching in a (Si,Ge)-mixed LCA-type first-neighbor (1) environment ( $x \approx 1$ , mode  $a_1$ , 460 cm<sup>-1</sup>). For the bottom  $(\text{Si} - \text{Si})_1^{\text{Ge}}$  branch due to Si-Si stretching in a full-Ge (1) environment, we consider a Ge-like supercell with an isolated Si-Si bond, searching for its stretching mode ( $x \approx 1$ , mode  $b_1$ , 464 cm<sup>-1</sup>), plus a Si-like supercell with an isolated Ge atom, being interested then in Si-Si stretching close to that impurity ( $x \approx 0$ , mode  $b_0$ , 502 cm<sup>-1</sup>).

TABLE I. *Ab initio* bond lengths, bulk moduli, and optical phonon frequencies of the pure Si and Ge crystals presently obtained with the SIESTA code, as compared with experimental values and with earlier *ab initio* values obtained with the AIMPRO code (cf. italics) (Ref. 48).

	Nearest-neighbor distance (Å)		Bulk modulus B (GPa)		$\omega_0$ (cm <sup>-1</sup> )	
	<i>Ab initio</i>	Exp.	<i>Ab initio</i>	Exp.	<i>Ab initio</i>	Exp.
Si	2.089	2.327 <sup>b</sup>	100.4	99.9 <sup>c</sup>	522	520.2 <sup>e</sup>
	2.335 <sup>a</sup>		99.7 <sup>b</sup>		518.1 <sup>a</sup>	
Ge	2.183	2.443 <sup>b</sup>	70.1	78.1 <sup>d</sup>	304	300.7 <sup>e</sup>
	2.417 <sup>a</sup>		75.2 <sup>a</sup>		300.9 <sup>a</sup>	

<sup>a</sup>Reference 48.

<sup>b</sup>Reference 49.

<sup>c</sup>Reference 50.

<sup>d</sup>Reference 51.

<sup>e</sup>Reference 52.

In the Si-dilute limit ( $x \approx 1$ ), the two Si-Si stretching modes  $a_1$  and  $b_1$  converge to  $462 \text{ cm}^{-1}$  within less than  $2 \text{ cm}^{-1}$ , which is globally consistent with the trend observed in Fig. 2(a). However, in contrast with earlier calculations of Franz *et al.* (refer to Sec. V C of Ref. 17), we are not able to resolve the experimental splitting of  $\sim 9 \text{ cm}^{-1}$  between the two branches (see Fig. 2(b)). For more decisive insight, we turn to the Ge-dilute limit ( $x \approx 0$ ), where the splitting is expected to be much larger, i.e.,  $\sim 30 \text{ cm}^{-1}$ , based on the experimental observations of Brya.<sup>15</sup> Our *ab initio* calculations reveal a distinct Si-Si stretching mode close to the isolated Ge ( $b_0$ ), the vibration pattern is schematically represented in Fig. 6(b). This emerges  $\sim 502 \text{ cm}^{-1}$ , i.e.,  $\sim 20 \text{ cm}^{-1}$  below the bulklike Si-Si stretching far from Ge ( $a_0$ ), in reasonable agreement with experimental findings (see Fig. 2(a)). For completeness, we extended the *ab initio* calculations to the localized stretching mode of a Si-Si bond taken between two Ge impurities in a Si-like matrix ( $x \approx 0$ ), so as to form a pseudolinear  $\dots\text{SiGe}(\text{SiSi})\text{GeSi}\dots$  chain immersed in Si. Again, such a mode is expected to refer to  $b_0$  in principle (see the basic representation of motif b in the body of Fig. 4). The phonon frequency of this mode is identified at  $502 \text{ cm}^{-1}$ , ideally matching the predicted value. Again, in the latter additional test, the *ab initio* calculations are strictly constrained to 1D, not to 3D, so as to remain fully consistent with the LCA upon which the 1D percolation scheme relies. Altogether, the preceding series of *ab initio* insights supports the 1D-cluster assignment of the Si-Si doublet.

## 2. Si-Ge spectral range

In principle, an insight into six limit frequencies is required to test the basic 1-bond  $\rightarrow$  3-mode Si-Ge pattern, if we omit the decomposition of the  $(\text{Si} - \text{Ge})_2^{\text{Si}}$  branch. However, our limitation to simple impurity motifs, so as to fulfill a basic condition regarding the convergence of our *ab initio* calculations (explained earlier), excludes the analysis of those Si-Ge branches referring to 1D environments formed with impurities only, such as  $(\text{Si} - \text{Ge})_2^{\text{Si}}$  near  $x \approx 1$  and  $(\text{Si} - \text{Ge})_2^{\text{Ge}}$  near  $x \approx 0$ . The remaining four limit frequencies are accessed by using two symmetrical pairs of impurity motifs. An isolated Si atom in Ge gives access to Si-Ge stretching in a full-Ge environment ( $x \approx 1$ , mode  $e_1$ ,  $385 \text{ cm}^{-1}$ ), corresponding to the LVM of Si in Ge. Its counterpart on the Si side, i.e., the Ge-LVM, is likewise accessed by considering an isolated Ge

atom in Si, focusing on the actual impurity vibration ( $x \approx 0$ , mode  $c_0$ ,  $451 \text{ cm}^{-1}$ ). The limit frequencies of the intermediate Si-Ge branch, due to Si-Ge stretching in a (Si,Ge)-mixed environment, are determined using a pair of impurities in second-neighbor positions, searching for the in-pair impurity stretching against the intermediate host atom (refer to the  $d_0$  and  $d_1$  modes at  $401$  and  $400 \text{ cm}^{-1}$ , respectively).

Altogether, each branch benefits from at least one *ab initio* insight, and the related frequencies match remarkably well the limit frequencies of the three Si-Ge branches near  $x \approx 0$  or  $x \approx 1$ . This secures the Si-Ge 1D-cluster pattern. The  $d_1$ - $e_1$  splitting  $\sim 400 \text{ cm}^{-1}$  has already been identified by Franz *et al.*,<sup>17</sup> using a different motif for  $d_1$ . In contrast, the  $d_0$ - $e_0$  counterparts remained unexplored so far. As we anticipated (see Sec. III A), the Ge-LVM  $c_0$  and Si-LVM  $e_1$  are connected with the top and bottom Si-Ge branches, respectively, not with the central or main one. In particular, near  $x \approx 0$ , where the two Si-Ge branches are well separated, the central or main Si-Ge branch unambiguously extrapolates to  $d_0$  (see Fig. 2(a)). This brings decisive insight into the nature of this branch, solving at the same time the long-standing enigma raised up by Brya.<sup>15</sup>

## 3. $(\text{Si-Ge})_2^{\text{Si}}$ fine structure

The presumed collapse of the  $(\text{Si} - \text{Ge})_2^{\text{SiGe}}$  branch into a pseudodoublet away from  $x \approx 0$  cannot be checked directly via our present *ab initio* calculations, as discussed previously. For preliminary insight, we refer to the dominant vibration patterns sketched in the body of Fig. 2(b), as identified by Grein and Cardona.<sup>20</sup> In each case, the bond stretching is emphasized by an oval for clarity. As expected, the extreme  $(1, 2_1)$  and  $(4_2, 5_1)$  pairs of vibration patterns basically refer to Si-Ge and Si-Si stretching, respectively. Moreover, in each case, the phonon frequency increases when the local environment becomes more Si-like. This is consistent with our generic 1D-cluster assignment of such doublets in terms of  $[(\text{Si} - \text{Ge})_2^{\text{Ge}}, (\text{Si} - \text{Ge})_2^{\text{SiGe}}]$  and  $[(\text{Si} - \text{Si})_1^{\text{Ge}}, (\text{Si} - \text{Si})_1^{\text{SiGe+Si}}]$ , respectively. The key question then is whether the features between, corresponding to the vibration patterns  $(3_1, 4_1)$ , basically refer to Si-Ge stretching, as we presume, or to Si-Si stretching. Clearly, both patterns refer to Si-Ge stretching (see the ovals) in a Si-like environment (pay attention to the local composition), the environment being more Si rich for the upper branch, as anticipated (see

Sec. III A). Apparently this conforms to our view that such modes basically proceed from the original  $(\text{Si} - \text{Ge})_2^{\text{Si}}$  branch.

#### 4. Ge-Ge spectral range

The two limit frequencies of the apparently unique Ge-Ge branch are accessed by considering a pure-Ge supercell ( $x \approx 1$ , mode  $f_1$ ,  $304 \text{ cm}^{-1}$ ), plus a Si-like supercell containing a pair of first-neighbor Ge impurities, searching then for the Ge-Ge stretching ( $x \approx 0$ , mode  $f_0$ ,  $281 \text{ cm}^{-1}$ ). The as-obtained *ab initio* values match the experimental ones within less than  $5 \text{ cm}^{-1}$ .

We have run further *ab initio* calculations in search of a possible extra Ge-Ge mode. In doing so, we considered a Ge-like supercell containing a unique Si impurity, in reference to the symmetrical supercell successfully used to evidence the  $a_0$ - $b_0$  splitting for Si-Si. The Si-induced tensile strain generates local Ge-Ge stretching near Si at significantly lower frequency ( $x \approx 1$ , unlabeled mode,  $\sim 280 \text{ cm}^{-1}$ ) than the bulklike Ge-Ge stretching far off Si ( $x \approx 1$ , mode  $f_1$ ,  $304 \text{ cm}^{-1}$ ), as schematically indicated in Fig. 4 (refer to the bottom arrow on the right side of the figure). The vibration pattern of such Ge-Ge stretching close to Si is identical to that found for the local Si-Si mode  $b_0$  close to an isolated Ge atom in Si, as schematically represented in Fig. 6(b). We deduce that the single-mode Ge-Ge behavior apparent in the Raman spectra may not be intrinsic but due to a screening of an actual multimode pattern similar to the Si-Si one. The reason the Ge-Ge Raman signal does not develop into a proper multimode pattern is not yet clear. We simply note along with Rath *et al.*<sup>16</sup> that the Ge-Ge spectral range is quasiconstantly blurred by a parasitical disorder-induced phonon density of states. This materializes into a distinct quasiamorphous ( $q$ - $a$ , refer to Fig. 1) band covering a broad frequency range ( $120$ - $310 \text{ cm}^{-1}$ ) from low Si content (see Fig. 2 of Ref. 16).

In brief, our simple frequency-based *ab initio* protocol, as focused on the bond-stretching modes along selected 1D-like impurity motifs, secures the intensity-based 1D-cluster assignment of the phonon branches (see Sec. III A) reported in Fig. 4. Furthermore, it reveals a predisposition of the Ge-Ge bond to exhibit a multimode Raman pattern, like Si-Si. However, this seems to be hampered by parasitical disorder-induced effects. Additional *ab initio* phonon calculations, not restricted to 1D-like impurity motifs, would be useful to provide a final answer to the problem of the fine-feature assignment of the SiGe Raman spectra or simply to refine the present 1D-cluster scheme. For example, the apparent decomposition of the  $(\text{Si} - \text{Ge})_2^{\text{Si}}$  mode into a pseudodoublet far off the Ge-dilute limit has not yet been firmly established.

#### C. Contour modeling of the Raman lineshapes within the 1D-cluster scheme

An overview of the 1D-cluster Raman lineshapes of the random  $\text{Si}_{1-x}\text{Ge}_x$  alloy is derived by taking the imaginary part of a sum of six Lorentzian functions representing the six basic [ $1 \times (\text{Ge-Ge})$ ,  $3 \times (\text{Si-Ge})$ ,  $2 \times (\text{Si-Si})$ ] harmonic oscillators, using the frequency (solid lines) and intensity (in reference to the fractions of oscillators specified on top of each branch) information available per oscillator in Fig. 4. In the case of the central  $(\text{Si} - \text{Ge})_2^{\text{SiGe}}$  line, whose frequency

shift vs composition significantly deviates from linearity when  $x < 0.4$ , we substitute to the crude linear curve corresponding to the plain line in Fig. 2(a) an empirical one obtained by interpolation of the abundant experimental data. In addition, we neglect the decomposition of the  $(\text{Si} - \text{Ge})_2^{\text{Si}}$  branch away from the Ge-dilute/moderate limit, where the contribution of this mode to the overall Raman signal becomes negligible.

The fractions of 1D oscillators merely act as weighting factors, applying to the intrinsic Si-Si, Si-Ge, and Ge-Ge Raman efficiencies. These remain to be determined. Experimental probing is problematic, because the perfect zincblende SiGe crystal, formed with Si-Ge bonds only, does not exist. We thus turn to a direct *ab initio* calculation of the Raman spectra of the diamond Si and Ge crystals and of the zincblende SiGe compound. These calculations are done by using a pseudopotential spin density-functional supercell code (AIMPRO),<sup>53</sup> along the lines of the local exchange-correlation parameterization by Perdew and Wang,<sup>54</sup> taking the potentials for Si and Ge as proposed by Hartwigsen *et al.* (Ref. 55). In doing so, we follow the exact procedure optimized earlier for SiGe in Ref. 48. Supercells of the same size were used for the three types of crystals for a direct comparison of the intrinsic (Ge-Ge, Si-Ge, Si-Si) Raman efficiencies. The resulting Si, Ge, and SiGe *ab initio* Raman spectra, uniformly damped for a direct comparison of the Raman efficiencies via the Raman intensities, are reported in the inset of Fig. 5. These scale approximately as (1, 2/3, 1/2).

The only remaining parameter for the calculation of the Raman spectra of the disordered SiGe alloy within the 1D-cluster scheme is the phonon damping per mode. This refers to the linewidth at half height of the corresponding Raman line. We use the composition dependencies of the linewidths of the main Ge-Ge ( $\gamma_{\text{Ge-Ge}}$ ), Si-Ge ( $\gamma_{\text{Si-Ge}}$ ), and Si-Si ( $\gamma_{\text{Si-Si}}$ ) Raman lines, as measured by Brya over extended composition domains (refer to Fig. 2 of Ref. 15). Such a systematic study of the SiGe phonon dampings covering simultaneously the Ge-Ge, Si-Ge, and Si-Si spectral ranges and large composition domains is quite unique in the literature. The available data suggest linear composition dependencies of the Ge-Ge and Si-Si linewidths, corresponding to  $\gamma_{\text{Ge-Ge}} \sim (-12.5x + 15.0) \text{ cm}^{-1}$  for  $x \lesssim 0.7$  and  $\gamma_{\text{Si-Si}} \sim (5.0x + 3.0) \text{ cm}^{-1}$  for  $x \lesssim 0.5$ , respectively. For our use, we extrapolate such linear trends over the full composition domain, in a crude approximation. Interestingly, Brya could detect the main Si-Ge line throughout the entire composition domain.<sup>15</sup> The Si-Ge linewidth  $\gamma_{\text{Si-Ge}}$  appears to remain quasistable at the two ends of the composition domain, i.e., corresponding to  $\gamma_{\text{Si-Ge}} \sim 8 \text{ cm}^{-1}$  near  $x \lesssim 0.5$  and to  $\gamma_{\text{Si-Ge}} \sim 12 \text{ cm}^{-1}$  near  $x \lesssim 0.7$ , and varies linearly between. In a crude approximation, we take identical linewidths for the like Raman lines of a given 1D-cluster multiplet, simply because such lines ultimately refer to the same bond stretching. Experimental support arises in that the like Si-Si (see Fig. 3(a)) and Si-Ge (Fig. 3(b) and 3(c)) Raman peaks exhibit similar linewidths when they coexist with similar intensities.

A representative set of as-obtained 1D-cluster Raman lineshapes for random  $\text{Si}_{1-x}\text{Ge}_x$  is displayed in Fig. 5. Globally, our calculated curves compare fairly well with the experimental ones, referring to the extended sets of Raman data independently collected at well-spanned alloy compositions

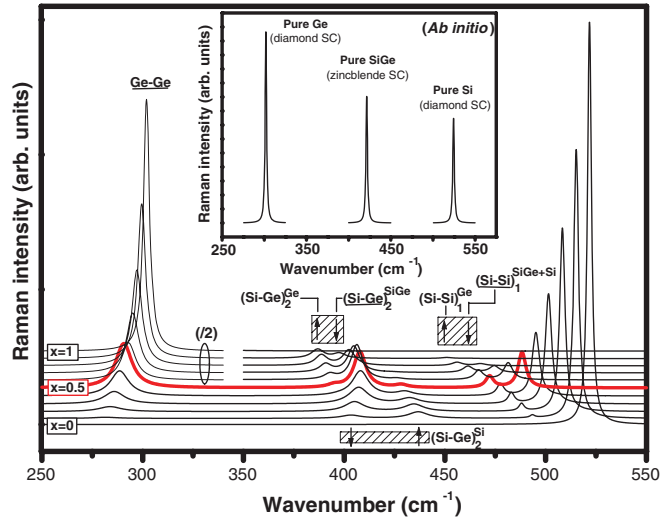


FIG. 5. (Color online) 1D-cluster SiGe Raman lineshapes. Reference 1D-cluster Raman lineshapes for random  $\text{Si}_{1-x}\text{Ge}_x$  as derived by taking the imaginary part of a classical six-oscillator  $[1 \times (\text{Ge-Ge}), 3 \times (\text{Si-Ge}), 2 \times (\text{Si-Si})]$  dielectric function, using the phonon frequencies (solid black lines) and fractions of oscillators (as specified on top of each branch) available in Fig. 4. The interval of alloy composition between consecutive curves corresponds to  $\delta x = 0.1$ . In the case of the central Si-Ge line, the composition dependence of the phonon frequency is directly interpolated from the abundant experimental data displayed in Fig. 2(a) for more realistic insight. Decomposition of the  $(\text{Si} - \text{Ge})_2^{\text{Si}}$  mode is neglected in a first approximation. The fractions of oscillators, which monitor the Raman intensities, merely act as weighting factors, applying to the Ge-Ge, Si-Ge, or Si-Si intrinsic Raman efficiencies (see text). The latter are determined from *ab initio* calculation of the Raman spectra of pure Ge (diamond), Si (diamond), and SiGe (zincblende) supercells (SCs) with the same size. The corresponding curves are displayed in the inset, using the same phonon damping for a direct comparison of the Raman efficiencies via the Raman intensities. In the main panel, the individual Ge-Ge, Si-Ge, and Si-Si phonon dampings are taken identical to those measured by Brya for the corresponding main lines (refer to fig. 2 of Ref. 15), assuming the same damping for the like Raman lines of a given 1D-cluster multiplet (Si-Ge or Si-Si) at a given alloy composition.  $\text{RI}_{1-2-3}$  between like Raman lines of a given 1D-cluster multiplet are emphasized by hatched areas (refer to Fig. 3 for a comparison with the experiment).

by Brya (see Fig. 1 of Ref. 15), by Alonso and Winer (as reproduced in Fig. 1 of this work), by Rath *et al.* (see Fig. 1 of Ref. 16), and by Pezzoli *et al.* (see Fig. 1 of Ref. 13). No adjustable parameter is used in our calculations. For example, the reference experimental signal near  $x \approx 0.5$ , corresponding to comparable intensities of the main Ge-Ge, Si-Ge, and Si-Si Raman features, is well reproduced. In addition, the RIs near  $x_{c1} \approx 0.70$  ( $\text{RI}_1$ ),  $x_{c2} \approx 0.90$  ( $\text{RI}_2$ ), and  $x_{c3} \approx 0.10$  ( $\text{RI}_3$ ), as pointed out by the shaded areas and opposite arrows in Fig. 5, are naturally accounted for.

More precisely, the comparison between the experimental and the theoretical curves is straightforward in the Ge-poor half of the composition domain ( $x \leq 0.6$ ), because the available experimental data mentioned previously converge to stable trends, irrespective of the types of samples used. The intensity ratios of the main Ge-Ge, Si-Ge, and Si-Si

lines are reproducible from one set of data to another one. In contrast, there exists considerable variation among the available experimental spectra in the Ge-rich half of the composition domain ( $x > 0.6$ ), where the Ge-Ge Raman line becomes largely dominant. The theory vs experiment comparison is thus more uncertain. For example, if we focus on the representative range of Ge content  $\sim 77$  at.%, the intensity ratio between the main Si-Ge mode and the dominant Ge-Ge mode varies as much as 2:3 ( $x = 0.77$ , epitaxial layers grown by liquid-phase epitaxy, Ref. 9 and Fig. 1 of the present work), 1:2 ( $x = 0.70$ , epitaxial layers deposited by molecular beam epitaxy, Ref. 16), 1:3 ( $x = 0.80$ , bulk polycrystals, Ref. 15), and 1:5 ( $x = 0.85$ , epilayers obtained by using the so-called low-energy plasma-enhanced chemical vapor deposition technique, Ref. 13). This may be due to a considerable variation in the value of the Ge-Ge phonon damping depending on the type of samples used. The damping values recently measured by Rath *et al.* with their extended set of epitaxial layers (see Fig. 5 of Ref. 16), corresponding to the composition dependence  $\gamma_{\text{Ge-Ge}} \sim (-12.5x + 23.5)\text{cm}^{-1}$ , overestimate by a factor as large as  $\sim 1.6$  the original values found by Brya with polycrystals (see Fig. 2 of Ref. 15).

In addition, the Si-Ge phonon damping is largely overestimated in our calculations, at least in the Ge-rich half of the composition domain, with concomitant impact on the intensity of the related Raman lines. This comes from a certain ambivalence of the dominant Si-Ge Raman signal. In the Ge-poor half of the composition domain, this unambiguously consists of a unique Raman line, the central line of the 1D-cluster Si-Ge triplet, i.e.,  $(\text{Si} - \text{Ge})_2^{\text{SiGe}}$ , which appears as a distinct and well-resolved feature far off its  $(\text{Si} - \text{Ge})_2^{\text{Si}}$  satellite (Fig. 5). The situation is not as clear when entering the Ge-rich half of the composition domain. Within the 1D-cluster scheme, the Si-Ge Raman signal then consists of a doublet resulting from the added contributions of the main  $(\text{Si} - \text{Ge})_2^{\text{SiGe}}$  line and of its novel  $(\text{Si} - \text{Ge})_2^{\text{Ge}}$  satellite, which points out at a slightly lower frequency (Fig. 5). The damping value for each component of the Si-Ge doublet is smaller than that measured by Brya,<sup>15</sup> which refers to the doublet as a whole. This was neglected in our calculations.

The previously mentioned approximations have no impact on the RIs. They only modify the relative strengths of Raman lines due to distinct bond stretching, while the RIs take place between like Raman lines referring to the same bond stretching.

To summarize, despite its simplicity, our 1D-cluster scheme, based on random  $\text{Si} \leftrightarrow \text{Ge}$  substitution, provides a fair quantitative understanding of the natural complexity of the  $\text{Si}_{1-x}\text{Ge}_x$  Raman spectra in their composition dependence, apart from the  $(\text{Si} - \text{Ge})_2^{\text{Si}}$  decomposition. On the practical side, this brings the important information that clustering, as well as anticlustering, effects can be neglected in SiGe, as suggested earlier by Pezzoli *et al.* (Ref. 13).

#### IV. SIGE (DIAMOND) VERSUS GAASP (ZINCLENDE) VERSIONS OF THE PERCOLATION SCHEME

An interesting question, then, is how the present version of the 1D-cluster scheme for diamond SiGe compares with the current 1-bond  $\rightarrow$  2-TO version of a zincblende alloy. A

natural zincblende reference in this respect is GaAsP because of a lattice mismatch similar to that of SiGe, i.e.,  $\sim 3\text{--}4\%$ . The local relaxations are thus comparable, as are the microscopic strains. Precisely, it appears in retrospect that the microscopic strain is the crucial ingredient that governs the ordering of the like phonon sub-branches in the 1D-cluster doublets of all re-examined zincblende alloys so far (details are given later). Additional interest arises in that SiGe and GaAsP are highly contrasted regarding the dispersion of their optical modes. These are nearly dispersionless in GaAs ( $\sim 15\text{ cm}^{-1}$ , Ref. 56) and GaP ( $\sim 1.5\text{ cm}^{-1}$ , Ref. 57) and strongly dispersive in Si ( $\sim 60\text{ cm}^{-1}$ , Ref. 31) and Ge ( $\sim 30\text{ cm}^{-1}$ , Ref. 31). This offers a unique opportunity to appreciate the extent to which the dispersion effect might challenge the zincblende version of the 1D-cluster scheme, based on the sole microscopic strain effect.

A basic difference between the SiGe (see Fig. 4) and GaAsP (see Fig. 7 of Ref. 29) 1D-cluster schemes is the opposite order of the like phonon branches in each multiplet. If we consider the well-resolved Ga-P doublet of GaAsP, the low-frequency (high-frequency) branch refers to the host region mainly formed with the short (long) bond, i.e., the GaP-like (GaAs-like) one. In contrast, the like phonon branches in each of the Si-Ge and Si-Si multiplets are ranked from bottom to top in the sense of more Si-rich host environments, as mainly formed with short Si-based bonds. Such Si-Si and Si-Ge inversions with respect to the reference Ga-P doublet are successively discussed hereafter.

#### A. Inversion of the Si-Si branches with respect to the reference Ga-P doublet: A dispersion effect discussed at the Si-parent limit ( $x \approx 0$ )

We tackle the issue of the Si-Si inversion with respect to Ga-P at the Si/GaP-parent limit ( $x \approx 0$ ), where the Si-Si doublet is best resolved, via *ab initio* calculations. The ultimate supercell providing simultaneous access to the two modes of a given doublet is a Si/GaP-like one containing a single Ge/As impurity, as sketched in Fig. 6(a). Our aim is to compare the lattice relaxation and dynamics of the host medium close to the impurity and far from it in the two systems after full relaxation of the supercells. The medium-related bond-length distributions and BZC-phonon curves of the (Ge,As)-doped (Si,GaP)-like supercells are shown in Fig. 6(a) and 6(b), respectively. Corresponding features in the two panels are identified using the same simplified labeling, with no subscript, for a direct link.

The  $(\text{Si-Si})^{\text{Ge}}/(\text{Ga-P})^{\text{As}}$  host bonds near the Ge/As impurity (refer to the superscript) suffer local compression due to the long (Ge-Si, Ga-As) impurity bonds (refer to the gray area around the isolated impurity in Fig. 6(a)). This gives rise to a distinct shoulder on the short-bond side of the main  $(\text{Si-Si})^{\text{Si}}/(\text{Ga-P})^{\text{P}}$  bulklike feature in Fig. 6(a). Transposed to the lattice dynamics (Fig. 6(b)), we would expect the host bonds close to the impurity to generate a distinct localized phonon at a higher frequency than the BZC-like ( $q \approx 0$ ) mode from the bulk. Indeed, an intuitive rule at 1D is that *the force constant of a bond reinforces when the bond is shortened, leading to hardening (blue-shift) of the phonon mode, and vice versa*. This is so for GaAsP, where the blue-shift is on the order of  $10\text{ cm}^{-1}$ , but not for SiGe, where a red-shift of  $\sim 25\text{ cm}^{-1}$  is detected

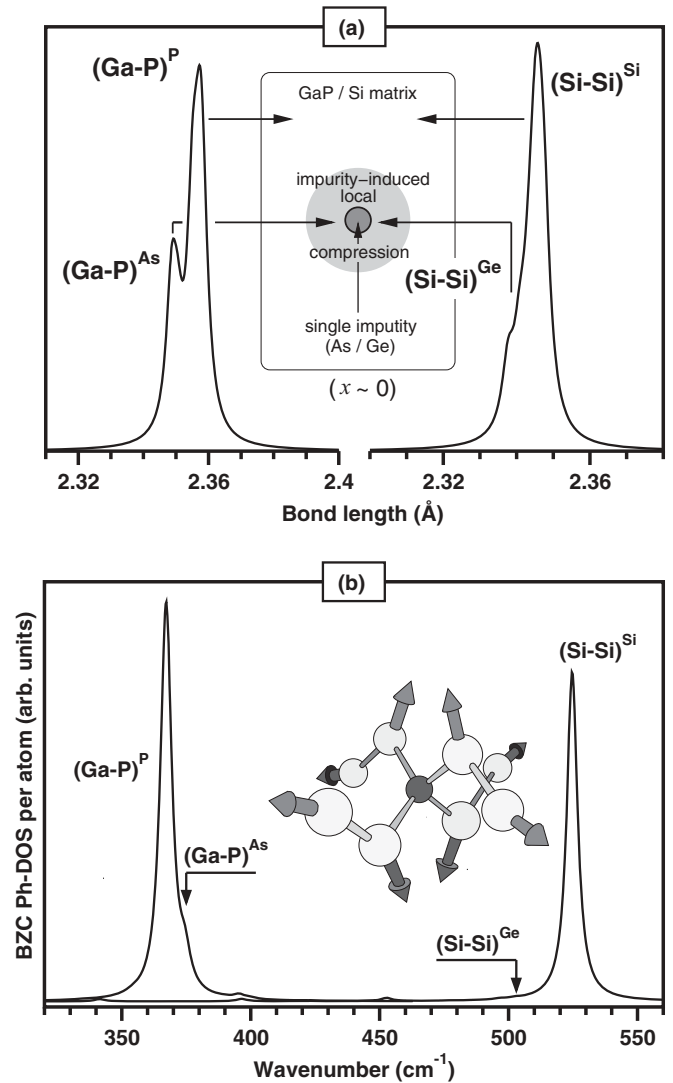


FIG. 6. SiGe (diamond) vs GaAsP (zincblende) comparison. Inversion of the Si-Si doublet: (a) *Ab initio* bond-length distributions and (b) phonon density of states at the Brillouin zone-center (BZC Ph-DOS) referring to the host Ga-P and Si-Si bonds of similar GaP- and Si-like (left and right, respectively) supercells containing a unique As/Ge impurity ( $x \approx 0$ ), as sketched in panel (a). The isolated As/Ge impurities produce a local compression of the host medium, as schematically represented by the gray area. The *ab initio* vibration pattern of the corresponding localized matrix-like  $(\text{Ga-P})^{\text{As}}/(\text{Si-Si})^{\text{Ge}}$  modes (in reference to  $b_0$  in Fig. 4 for SiGe) is schematically represented in panel (b). The host atoms beyond the second neighbors of the impurity (not shown) remain motionless. Corresponding bond-length and phonon features in panels (a) and (b), respectively, are labeled using the same simplified 1D-cluster terminology, with no subscript, for a direct link.

instead. Such an apparent anomaly for SiGe can be explained only if the compression-induced hardening effect (blue-shift) is compensated for by a larger confinement-induced softening effect (red-shift).

As extensively discussed by Rucker and Methfessel (Ref. 3), the central idea behind the confinement effect is that the host medium constitutes an obstacle to the propagation of a “foreign” (impurity) mode, simply because it does

not naturally vibrate at the same frequency. Therefore, the impurity mode remains confined onto the impurity motif. As such, it cannot be described in terms of a nominal  $q \approx 0$  Raman-allowed mode, corresponding to a quasi-infinite correlation length. It is currently decomposed into a series of elementary plane waves involving disorder-induced theoretically forbidden  $q \neq 0$  modes. A dominant  $q \approx 0$  (BZC) character is nevertheless presumed, corresponding to out-of-phase vibration (optical character) of the two intercalated *fcc* sublattices taken as quasirigid (BZC character). Such a picture has been formalized into the well-known spatial correlation model (SCM),<sup>58,59</sup> in which the series runs over all possible  $q$  values from the BZC to the Brillouin zone edge (BZE), with decreasing weight of the elementary modes when  $q$  gets closer to the BZE. In most semiconductors, the optical phonons exhibit negative dispersion, so the confinement effect usually leads to a red-shift with respect to the nominal BZC mode of a pure crystal.

Such a drastic red-shift as  $\sim 25 \text{ cm}^{-1}$  cannot be explained within the SCM, i.e., by assuming that the impurity mode retains a dominant BZC-like character. Indeed, even for confinement of the highly dispersive Si-Si optical mode at the ultimate scale of the lattice constant, the red-shift predicted by the SCM does not exceed  $\sim 5 \text{ cm}^{-1}$  (see Fig. 1 of Ref. 58).

The only way to take full advantage of the phonon dispersion is to suppose that the localized Si-Si impurity mode behaves more like a BZE mode than like a BZC one. Just such a BZE mode can be identified via its vibration pattern, considering that not only the two *fcc* sublattices (optical character) but also the first neighbors on each *fcc* sublattice (BZE character) should vibrate out of phase. For a direct insight, we sketched in Fig. 6(b) the *ab initio* vibration pattern of the Si-Si stretching mode close to Ge. We checked that the Ga-P vibration pattern close to As is similar. The atom displacements are negligible beyond the second neighbors of the isolated impurity (not shown), which establishes the local character of such impurity-induced modes. Furthermore, we observe that the Si (P) atoms immediately connected to the isolated Ge (As) impurity, thus located on the same *fcc* sublattice, exhibit two-to-two antiphase displacements. The same holds true for the Si/P atoms sitting in second-neighbor positions on the same Ge/As-like *fcc* sublattice. Altogether, this testifies to an effective BZE-like character of the Si-Si and Ga-P local modes close to the Ge/As impurities, as expected.

The dispersion-induced phonon softening is maximum for BZE phonons, i.e., of the same order of magnitude as the BZC-BZE dispersion. In the case of GaAsP, the hardening effect due to the impurity-induced compressive strain is not challenged, due to the absence of Ga-P dispersion. In contrast, the dispersion-induced softening should easily screen the strain-induced hardening in SiGe, a rather moderate one (i.e., merely of  $\sim 10 \text{ cm}^{-1}$ ), if we refer to GaAsP because of the large Si dispersion ( $\sim 60 \text{ cm}^{-1}$ ). In this case, the Si-Si local mode near Ge (BZE-like) would fall over the Si-Si parent-like one far off Ge (BZC-like) when  $x \approx 0$ . This, we believe, is the origin of the spectacular Si-Si inversion with respect to Ga-P at the Si-parent limit.

When departing from this limit, both the lower and the upper modes are red-shifted. This is because, first, the short

Si-Si bonds experience tensile strain due to the progressive dilation of the host lattice with Ge incorporation. At the same time, the upper mode, originally a BZC-like one, becomes increasingly confined, which, in turn, generates an additional red-shift, as accounted for by the SCM (explained earlier) and discussed in detail by Rucker and Methfessel (Ref. 3, see Sec. I). In contrast, the confinement of the lower mode, which is already maximum (BZE-like) near  $x \approx 0$ , remains basically invariant. Accordingly, the two modes progressively converge when  $x$  increases. A quasiperfect coincidence seems to be eventually achieved near  $x \approx 1$ , supported by our *ab initio* phonon calculations (refer to  $a_1$ - $b_1$  in Fig. 4). The two Si-Si branches are then represented by similar series of Si-impurity motifs, thus suffering comparable strain and dispersion effects.

### B. Inversion of the Si-Ge branches with respect to the reference Ga-P doublet: A lattice relaxation effect discussed at the Si-dilute limit ( $x \approx 1$ )

We now discuss the Si-Ge inversion with respect to Ga-P at a dilute limit. All Si-Ge modes are of the impurity type, thus suffering a similar dispersion effect. As such, the dispersion effect is virtually excluded from the discussion. Only the microscopic strain needs to be considered. Everything comes down to a comparison of the lattice relaxations in the zincblende (GaAsP) and diamond (SiGe) lattices, from the point of view of the dilute (Si-Ge)/(Ga-P) bonds. The lattice dynamics immediately follows in principle, using the basic rule highlighted with italics in the previous section. At the (Ga-P)-dilute limit, the short Ga-P bonds are dispersed into the GaAs-like host medium with a large lattice constant. The equivalent situation for the Si-Ge bond is achieved at the Si-dilute limit only, the minor Si-Ge bonds being shorter than the host Ge-Ge ones. The Si-Ge vs Ga-P confrontation is thus placed at this limit.

For a direct Si-Ge vs Ga-P comparison, we use impurity motifs that are transposable from the diamond structure to the zincblende one. An inevitable drawback is that this comparison is limited to the bottom and intermediate Si-Ge branches only. The top Si-Ge branch cannot be addressed, because the related impurity motif, i.e., a pseudolinear chain of five Si atoms with an intermediate Ge atom (see Fig. 4), does not transpose to the zincblende structure. In practice, we select those two motifs currently used to run the zincblende version of our *ab initio* protocol (see Sec. II). These consist of one isolated (Si/P) impurity (1 imp) plus one pair of second-neighbor impurities (2 imp), to be immersed in Ge/GaAs-like supercells. The impurity-related distribution of bond lengths and BZC-phonon curves after full relaxation of the supercells are shown in Fig. 7(a) and 7(b), respectively. Again, corresponding features in the two data sets are identified by using the same simplified labeling, with no subscript, for a direct link. As expected, there is a striking difference between the zincblende and the diamond lattice relaxations, with concomitant impact on the lattice dynamics.

The short Si-Ge bonds in Ge are shorter (clouds of dense dots) in the Si-rich (2-imp) region and longer (clouds of dispersed dots) in the Si-poor (1-imp) one (Fig. 7(a), right), thus vibrating at higher and at lower frequency (recall the

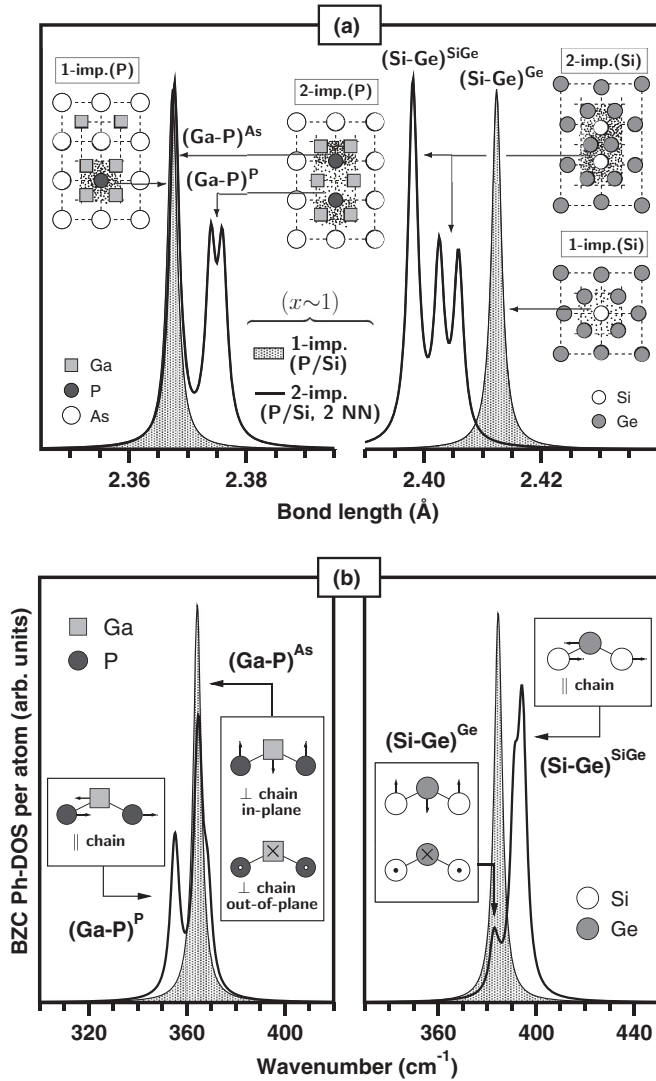


FIG. 7. SiGe (diamond) vs GaAsP (zincblende) comparison. Inversion of the Si-Ge multiplet: (a) *Ab initio* bond-length distributions and (b) phonon density of states at the Brillouin zone-center (BZC Ph-DOS), referring to the impurity bonds of similar GaAs- and Ge-like (left and right, respectively) supercells ( $x \approx 1$ ) containing either an isolated P/Si impurity (gray curves) or a pair of such impurities sitting in second-neighbor positions (clear curves), as sketched in panel (a). Clouds of dense and dispersed dots refer to shorter and longer impurity bonds, respectively. The situations are opposite for the GaAsP and SiGe schemes. Corresponding bond-length and phonon features—or set of features—in panels (a) and (b), respectively, are labeled using the same simplified 1D-cluster type terminology, with no subscript, for a direct link. In panel (b), only schematic vibration patterns are displayed, for a direct SiGe vs GaAsP comparison (qualitative). A standard notation is used for backward ( $\boxtimes$ ) or upward ( $\odot$ ) atomic motions.

basic rule in *italics* in Sec. IV A), respectively (Fig. 7(b), right). This conforms to intuition. Indeed, the connection of the Si-impurity motifs to the surrounding Ge-like matrix involves eight short Si-Ge bonds for 2 imp against four only for 1 imp. The Si-rich (2-imp) domain thus offers stronger resistance to the medium-induced tensile strain, and as such retains more efficiently the naturally short Si-Ge bond length.

Surprisingly, the trend is opposite for Ga-P, the short Ga-P bonds being longer (clouds of dispersed dots) inside the P-Ga-P (2-imp) chain and shorter (clouds of dense dots) at its extremities, or around an isolated P (1-imp) atom (Fig. 7(a), left), with concomitant impact on the Ga-P phonon frequencies (Fig. 7(b), left). The latter two series of Ga-P bonds exhibit similar bond length, indicating that the local relaxation outside a given P-impurity motif does not depend on the arrangement of the P atoms inside that motif. This is consistent with a current observation by extended  $x$ -ray absorption fine-structure measurements in zincblende alloys that the substituting *fcc* sublattice remains nearly undistorted.<sup>60–63</sup> The local strain is merely accommodated by a distortion of the invariant *fcc* sublattice. This was formalized into a model by Balzarotti *et al.* (Ref. 64). As the P atoms stay at the nodes of the undistorted *fcc* GaAs-like sublattice, with a large lattice constant, the local tensile strain inside the P–Ga–P (2-imp) motif can only be accommodated by a mere in-plane motion of the central Ga atom toward the P pair. Such relaxation is not as efficient as that achieved at the two extremities of the P–Ga–P chain or around the isolated P atom (1 imp), where three and four unconstrained Ga atoms are available per P atom, respectively. Accordingly, the former in-chain Ga-P bonds remain longer than the latter ones.

In summary, we attribute the opposite order of the Si-Ge and Ga-P branches to a difference in nature between the local lattice relaxations in the diamond and those in the zincblende alloys. In the first case, all sites are equivalent in the relaxation process, so an impurity motif tends to shrink or expand as a whole to retain the native bond lengths of its constituting species. In contrast, the zincblende relaxation process is constrained to a strict condition that the substituting *fcc* sublattice should remain undistorted. This suffices to generate a counterintuitive trend in the lattice relaxation that short bonds tend to be longer in their own environment than in the environment of the other (long) species, transposed onto the order of the two sub-branches of a 1D-cluster doublet. This, we believe, is the origin of the Si-Ge inversion with respect to Ga-P.

## V. CONCLUSION

A reactualized version of the phenomenological, *i.e.*, LCA-based, percolation scheme, which has recently led to a unification of the classification of the Raman spectra of the random III–V and II–VI  $A_{1-x}B_xC$  zincblende semiconductor alloys,<sup>28,29</sup> is applied to random  $\text{Si}_{1-x}\text{Ge}_x$ , the leading group IV semiconductor alloy with diamond structure. In this so-called 1D-cluster version, the current shortcomings regarding the assignment of the individual Raman lines, which relate to the composition and length scale of the 1D environment of a bond, are overcome.

RI within both the Si-Si ( $\text{RI}_1$ ) and the Si-Ge ( $\text{RI}_{2-3}$ ) spectral ranges when reaching the Si- and Ge-dilute/moderate limits, known from the literature, are used to reassign the individual SiGe Raman lines into a proper seven-oscillator [ $1 \times (\text{Ge-Ge})$ ,  $4 \times (\text{Si-Ge})$ ,  $2 \times (\text{Si-Si})$ ] version of the 1D-cluster scheme, assuming a random  $\text{Si} \leftrightarrow \text{Ge}$  substitution. This strongly deviates from the currently admitted six-oscillator [ $1 \times (\text{Ge-Ge})$ ,  $1 \times (\text{Si-Ge})$ ,  $4 \times (\text{Si-Si})$ ] picture. In particular, the Si-Ge

multimode pattern supported by the 1D-cluster version solves a long-standing enigma originally pointed out by Brya<sup>15</sup> as to why the presumably unique Si-Ge mode in the traditional assignment of the SiGe Raman lines does not converge onto the Ge-LVM or onto the Si-LVM when reaching the Ge- or Si-dilute limits, respectively.

The 1D-cluster reassignment of the SiGe Raman lines is independently secured by *ab initio* insight into the frequency of bond-stretching modes along prototype impurity motifs. These are taken as pseudolinear so as to remain consistent with the LCA, upon which the 1D-cluster scheme relies. Fair contour modeling of the multimode SiGe Raman lineshapes is eventually achieved on this basis after *ab initio* calibration of the intrinsic Ge-Ge, Si-Ge, and Si-Si Raman efficiencies and proper weighting of such efficiencies by the fractions of related multioscillators in the crystal. Such fractions are likewise estimated within the LCA, assuming a random Si↔Ge substitution. This result points out that clustering and ordering effects play a minor role in SiGe alloys, as suggested by Pezzoli *et al.* (Ref. 13). We mention, nevertheless, that additional fully 3D *ab initio* calculations would be useful to provide a final answer to the problem of the fine-structure assignment of the SiGe Raman spectra.

More precisely, a predisposition of the Ge-Ge bond to exhibit a multimode Raman pattern, as evidenced by *ab initio*, seems to be impeded by parasitical disorder-induced effects. A unique Raman mode is currently detected in the Ge-Ge spectral range, indicating a basic insensitivity of the Ge-Ge bond stretching to its local environment. In contrast, significant fine structuring exists for both Si-Si and Si-Ge bond stretching, revealing sensitivities to their first- and second-neighbor 1D

environments, respectively. However, none of these is able to discriminate among all possible variants of such environments. Si-Si merely distinguishes between all-Ge (bottom branch) and other environments (top branch), i.e., including at least one Si atom. Regarding Si-Ge, the extreme Raman features refer to all-Ge (bottom branch) and all-Si (top branch) environments, the other (mixed) ones providing a common feature between (intermediate branch). A decomposition of the top Si-Ge branch soon after departing from the Ge-moderate limit suggests some sensitivity beyond the second neighbors. Nevertheless, we are not able to identify the microstructure of such environments. For comparison, the zincblende version of the 1D-cluster scheme merely distinguishes between the two possible first-neighbor 1D environments of a bond, as discussed in this work.

Another major deviation between the SiGe and the zincblende versions of the 1D-cluster scheme, taking GaAsP as a reference, is concerned with an inversion of the order of the like phonon branches in each 1D-cluster multiplet. This is attributed either to the considerable phonon dispersion of the Ge and Si crystals (Si-Si doublet) or to a basic difference between the diamond and the zincblende lattice relaxations (Si-Ge triplet). The SiGe vs GaAsP comparison is supported by *ab initio* bond-length and BZC-phonon calculations using impurity motifs that are directly transposable from the zincblende structure to the diamond one.

Generally, this work constitutes the first extension of the percolation/1D-cluster scheme for the basic understanding of the Raman spectra of mixed crystals beyond the zincblende structure. We hope that it stimulates further extension to other crystal structures.

\*olivier.pages@univ-lorraine.fr

<sup>1</sup>S. Adachi, *Properties of Semiconductor Alloys, Group-IV, III-V and II-VI Semiconductors* (John Wiley & Sons, Chichester, UK, 2009).

<sup>2</sup>R. M. Martin, *Phys. Rev. B* **1**, 4005 (1970).

<sup>3</sup>H. Rucker and M. Methfessel, *Phys. Rev. B* **52**, 11059 (1995).

<sup>4</sup>E. A. Fitzgerald, Y.-H. Xie, M. L. Green, D. Brasen, A. R. Kortan, J. Michel, Y.-J. Mii, and B. E. Weir, *Appl. Phys. Lett.* **59**, 811 (1991).

<sup>5</sup>M. L. Lee and E. A. Fitzgerald, *J. Appl. Phys.* **94**, 2590 (2003).

<sup>6</sup>J. Welsler, J. L. Hoyt, and J. F. Gibbons, *IEEE Electron Device Lett.* **15**, 100 (1994).

<sup>7</sup>D. K. Nayak, J. C. S. Woo, J. S. Park, K. L. Wang, and K. P. MacWilliams, *Appl. Phys. Lett.* **62**, 2853 (1993).

<sup>8</sup>H. H. Burke and I. P. Herman, *Phys. Rev. B* **48**, 15016 (1993).

<sup>9</sup>M. I. Alonso and K. Winer, *Phys. Rev. B* **39**, 10056 (1989).

<sup>10</sup>M. I. Alonso, F. Cerdeira, D. Niles, M. Cardona, E. Kasper, and H. Kibbel, *J. Appl. Phys.* **66**, 5645 (1989).

<sup>11</sup>R. Schorer, G. Abstreiter, S. de Gironcoli, E. Molinari, H. Kibbel, and H. Presting, *Phys. Rev. B* **49**, 5406 (1994).

<sup>12</sup>Z. Sui, H. H. Burke, and I. P. Herman, *Phys. Rev. B* **48**, 2162 (1993).

<sup>13</sup>F. Pezzoli, L. Martinelli, E. Grilli, M. Guzzi, S. Sanguinetti, M. Bollani, H. D. Chrastina, G. Isella, H. von Känel, E. Wintersberger, J. Stangl, and G. Bauer, *Mater. Sci. Eng. B* **124-125**, 127 (2005).

<sup>14</sup>D. W. Feldman, M. Ashkin, and J. H. Parker Jr., *Phys. Rev. Lett.* **17**, 1209 (1966).

<sup>15</sup>W. J. Brya, *Solid State Comm.* **12**, 253 (1973).

<sup>16</sup>S. Rath, M. L. Hsieh, P. Etchegoin, and R. A. Stradling, *Semicond. Sci. Technol.* **18**, 566 (2003).

<sup>17</sup>M. Franz, K. F. Dombrowski, H. Rucker, B. Dietrich, K. Pressel, A. Barz, U. Kerat, P. Dold, and K. W. Benz, *Phys. Rev. B* **59**, 10614 (1999).

<sup>18</sup>P. G. Dawber and R. J. Elliott, *Proc. R. Soc. London A* **273**, 222 (1963).

<sup>19</sup>A. A. Maradudin, *Solid State Phys.* **18**, 273 (1966).

<sup>20</sup>C. H. Grein and M. Cardona, *Phys. Rev. B* **45**, 8328 (1992).

<sup>21</sup>S. de Gironcoli, *Phys. Rev. B* **46**, 2412 (1992).

<sup>22</sup>S. de Gironcoli and S. Baroni, *Phys. Rev. Lett.* **69**, 1959 (1992).

<sup>23</sup>E. W. Montroll and R. B. Potts, *Phys. Rev.* **100**, 525 (1955); E. W. Montroll and R. B. Potts, *ibid.* **102**, 72 (1956).

<sup>24</sup>M. A. Renucci, J. B. Renucci, and M. Cardona, in *Light Scattering in Solids*, edited by M. Balkanski (Flammarion, Paris, 1971), p. 326

<sup>25</sup>D. W. Taylor, in *Optical Properties of Mixed Crystals*, edited by R. J. Elliott and I. P. Ipatova (North-Holland, Amsterdam, 1988), Chap. 2, p. 85.

<sup>26</sup>I. F. Chang and S. S. Mitra, *Adv. Phys.* **20**, 359 (1971).

<sup>27</sup>H. W. Verleur and A. S. Barker Jr., *Phys. Rev.* **149**, 715 (1966).

<sup>28</sup>O. Pagès, J. Souhabi, A. V. Postnikov, and A. Chafi, *Phys. Rev. B* **80**, 035204 (2009).

- <sup>29</sup>O. Pagès, A. V. Postnikov, M. Kassem, A. Chafi, A. Nassour, and S. Doyen, *Phys. Rev. B* **77**, 125208 (2008).
- <sup>30</sup>For example, it may not be physically realistic within such a phenomenological model as the cluster model, thus operating within the LCA (i.e., at 1D), to assign elementary oscillators at 3D. Also, the basic idea behind the cluster model—that a given bond species in any cluster unit should provide a single Raman feature—is not physically realistic and is in contradiction with recent *ab initio* findings (Ref. 28).
- <sup>31</sup>P. Giannozzi, S. de Gironcoli, P. Pavone, and S. Baroni, *Phys. Rev. B* **43**, 7231 (1991).
- <sup>32</sup>O. Pagès, M. Ajjoun, D. Bormann, C. Chauvet, E. Tournié, and J. P. Faurie, *Phys. Rev. B* **65**, 035213 (2001).
- <sup>33</sup>O. Pagès, M. Ajjoun, T. Tite, D. Bormann, E. Torunié, and K. C. Rustagi, *Phys. Rev. B* **70**, 155319 (2004).
- <sup>34</sup>O. Pagès, T. Tite, A. Chafi, D. Bormann, O. Maksimov, and M. C. Tamargo, *J. Appl. Phys.* **99**, 063507 (2006).
- <sup>35</sup>W. Weber, *Phys. Rev. Lett.* **33**, 371 (1974); *Phys. Rev. B* **15**, 4789 (1977).
- <sup>36</sup>D. Stauffer and A. Aharony, *Introduction to Percolation Theory*, 2nd ed. (Taylor & Francis, London, 1991).
- <sup>37</sup>C. Vèrié, *J. Crystal Growth* **184/185**, 1061 (1998).
- <sup>38</sup>This brings us to imagine that the individual 1D oscillators (i.e.,  $C(AC)B$ ,  $C(AC)A$ ,  $C(BC)A$ , and  $C(BC)B$ ) are immersed into a VCA-like continuum, just like in the MREI and cluster models.
- <sup>39</sup>A. V. Postnikov, O. Pagès, and J. Hugel, *Phys. Rev. B* **71**, 115206 (2005).
- <sup>40</sup>G. K. Pradhan, C. Narayana, O. Pagès, A. Breidi, J. Souhabi, A. V. Postnikov, S. K. Deb, F. Firszt, W. Paszkowicz, A. Shukla, and F. El Haj Hassan, *Phys. Rev. B* **81**, 115207 (2010).
- <sup>41</sup>SiGe contains four such bond percolation thresholds, identifying with the critical alloy compositions  $x_{\text{Ge-Ge}} \approx 0.43$ ,  $x_{\text{Ge-Si}} \approx 0.25$ ,  $x_{\text{Si-Ge}} \approx 0.75$ , and  $x_{\text{Si-Si}} \approx 0.57$ . The two extreme values, symmetrical ones, are well known. They correspond to connections of the minor Ge and Si atoms into pseudoinfinite treelike chains running throughout the diamond lattice (Ref. 36). The intermediary values, also symmetrical ones, were recently determined by one of us using the breadth-first-search algorithm (R. Garg and K. C. Rustagi, [arXiv:0909.2922](https://arxiv.org/abs/0909.2922)). They refer to similar formations of pseudoinfinite chains of alternate Si and Ge atoms on one or the other of the two *fcc* sublattices forming the diamond lattice.
- <sup>42</sup>A current, and stronger, approximation with 3D approaches is equal polarizability for all atoms (Refs. 3, 17, 21, and 22).
- <sup>43</sup>A. M. Teweldeberhan and S. Fahy, *Phys. Rev. B* **73**, 245215 (2006).
- <sup>44</sup>For example, the frequency of the bending mode of the isolated Si-Si pair near  $x \approx 1$  (refer to the bottom spectrum in Fig. 10b in Ref. 17), whose stretching mode is nominally associated with the  $(\text{Si} - \text{Si})_1^{\text{Ge}}$  branch (refer to b1 in Fig. 4), coincides within less than  $2 \text{ cm}^{-1}$  with the frequency of Si-Ge bond stretching along the pseudolinear Si-Ge-Si motif, which is nominally associated with the  $(\text{Si} - \text{Ge})_2^{\text{SiGe}}$  branch (refer to d<sub>1</sub> in Fig. 4).
- <sup>45</sup>D. M. Ceperley and B. J. Alder, *Phys. Rev. B* **36**, 2092 (1987).
- <sup>46</sup>J. M. Soler, E. Artacho, J. D. Gale, A. Garcia, J. Junquera, P. Ordejón, and D. Sanchez-Portal, *J. Phys. Condens. Matter* **14**, 2745 (2002).
- <sup>47</sup>N. Troullier and J. L. Martins, *Phys. Rev. B* **43**, 1993 (1991).
- <sup>48</sup>V. J. B. Torres, J. Coutinho, P. R. Briddon, and M. Barroso, *Thin Solid Films* **517**, 395 (2008).
- <sup>49</sup>M. C. Ridgway, K. M. Yu, C. J. Glover, G. J. Foran, C. Clerc, J. L. Hansen, and A. N. Larsen, *Phys. Rev. B* **60**, 10831 (1999).
- <sup>50</sup>B. A. Weinstein and G. Piermarini, *Phys. Rev. B* **12**, 1172 (1975).
- <sup>51</sup>D. Olego and M. Cardona, *Phys. Rev. B* **25**, 1151 (1982).
- <sup>52</sup>T. P. Mernagh and L. G. Liu, *J. Phys. Chem. Solid.* **52**, 507 (1991).
- <sup>53</sup>P. R. Briddon and R. Jones, *Phys. Status Solidi B* **207**, 131 (2000).
- <sup>54</sup>J. P. Perdew and Y. Wang, *Phys. Rev. B* **45**, 13244 (1992).
- <sup>55</sup>C. Hartwigsen, S. Goedecker, and J. Hutter, *Phys. Rev. B* **58**, 3641 (1998).
- <sup>56</sup>D. Strauch and B. Dorner, *J. Phys. Condens. Matter* **2**, 1457 (1990).
- <sup>57</sup>H. Fu, V. Ozoliņš, and A. Zunger, *Phys. Rev. B* **59**, 2881 (1999).
- <sup>58</sup>H. Richter, Z. P. Wang, and L. Ley, *Solid State Comm.* **39**, 625 (1981).
- <sup>59</sup>I. H. Campbell and P. M. Fauchet, *Solid State Comm.* **58**, 739 (1986).
- <sup>60</sup>Z. Wu, K. Lu, Y. Wang, J. Dong, H. Li, Ch. Li, and Z. Fang, *Phys. Rev. B* **48**, 8694 (1993).
- <sup>61</sup>J. C. Mikkelsen Jr., and J. B. Boyce, *Phys. Rev. B* **28**, 7130 (1983).
- <sup>62</sup>J. Pellicer-Porres, A. Polian, A. Segura, V. Muñoz-Sanjósé, A. Di Cicco, and A. Traverse, *J. Appl. Phys.* **96**, 1491 (2004).
- <sup>63</sup>T. Ganguli, J. Mazher, A. Polian, S. K. Deb, F. Villain, O. Pagès, W. Paszkowicz, and F. Firszt, *J. Appl. Phys.* **108**, 083539 (2010).
- <sup>64</sup>A. Balzarotti, N. Motta, A. Kisiel, M. Zimnal-Starnawska, M. T. Czyżyk, and M. Podgórný, *Phys. Rev. B* **31**, 7526 (1985).